Czech Technical University in Prague

Faculty of Electrical Engineering
Department of Electromagnetic Field

Master thesis

Antenna for Microwave Imaging Methods in Medicine

Širokopásmová anténa pro mikrovlnné zobrazovací metody v medicíně

Author: Bc. Vojtěch Hrubý

Supervisor: prof. Ing. Jan Vrba, CSc.   May 2019

I. OSOBNÍ A STUDIJNÍ ÚDAJE

Příjmení: **Hrubý**   Jméno: **Vojtěch**   Osobní číslo: **407255**

Fakulta/ústav: **Fakulta elektrotechnická**

Zadávající katedra/ústav:

Studijní program: **Elektronika a komunikace**

Studijní obor: **Rádiová a optická technika**

II. ÚDAJE K DIPLOMOVÉ PRÁCI

Název diplomové práce:

Širokopásmová anténa pro mikrovlnné zobrazovací metody v medicíně

Název diplomové práce anglicky:

Antenna for Microwave Imaging Methods in Medicine

Pokyny pro vypracování:

Prostudujte odbornou literaturu o návrhu širokopásmových (UWB) antén s ohledem na možnost jejich využití v aplikátorech pro mikrovlnné zobrazovací systémy na bázi UWB radaru. Vyberte anténu, která by byla vhodným prvkem pro aplikátor určený pro neinvazivní měření změny teploty při mikrovlnné hypertermii.
Simulujte vlastnosti vybraného typu UWB antény pro mikrovlnné zobrazování v simulátoru elektromagnetického pole. Vlastnosti této UWB antény optimalizujte na numerickém fantomu svalové tkáně. Modul parametru S11 by ve frekvenčním pásmu 1-3 GHz neměl být vyšší než – 10 dB.
Navrženou UWB anténu realizujte a otestujte, tj. změřte její činitel odrazu ve frekvenčním pásmu 1 až 3 GHz. Při pracovní frekvenci 2,45 GHz pak změřte 3D distribuci SAR a rozložení teploty v homogenním agarovém fantomu.

Seznam doporučené literatury:

[1] Vrba, J.: „Lékařské aplikace mikrovlnné techniky". Skriptum ČVUT-FEL, Praha, 2007
[2] Vrbajr, J.: „ Perspective medical diagnostics methods based on microwave measurement of dielectric properties of biological tissues". Habilitační práce ČVUT-FBMI, Kladno, 2017
[3] Vrba, D.: "Perspective use of MTM applicators in clinical practise". Habilitační práce ČVUT-FBMI, Kladno, 2018
[4] Fišer, O.: „Microwave hyperthermia for treatment of head and neck tumors controlled by non-invasive temperature monitoring based on UWB radar". Disertační práce ČVUT-FEL, Praha, 2018

Jméno a pracoviště vedoucí(ho) diplomové práce:

prof. Ing. Jan Vrba, CSc.,   katedra elektromagnetického pole   FEL

Jméno a pracoviště druhé(ho) vedoucí(ho) nebo konzultanta(ky) diplomové práce:

Datum zadání diplomové práce: **09.10.2018**   Termín odevzdání diplomové práce: **24.05.2019**

Platnost zadání diplomové práce:
do konce letního semestru 2019/2020

_____   _____   _____
prof. Ing. Jan Vrba, CSc.   podpis vedoucí(ho) ústavu/katedry   prof. Ing. Pavel Ripka, CSc.
podpis vedoucí(ho) práce   podpis děkana(ky)

Declaration of originality

I, the undersigned, hereby declare that I have developed diploma thesis "Antenna for Microwave imaging Methods in Medicine" on my own and that the statement of resources presented in this work is a complete statement of all resources used.

In Prague on   signature

Acknowledgements

I want to express my gratitude to my master's thesis supervisor prof. Ing. Jan Vrba, CSc. who introduced me into the subject of medical applications of an electromagnetic field and supervised my bachelor and diploma thesis. His remarks during this master's thesis were beneficial and inspiring. Furthermore, I would like to thank my parents, who have always supported and motivated me during my university studies.

Abstract

This master's thesis deals with the design of an ultra-wideband (UWB) antenna for microwave imaging methods in medicine. The design of a planar bow-tie antenna with planar tapered balun feeder is presented. Proposed antenna geometry is optimized by simulating antenna structure using FDTD solver. The proposed antenna is fabricated, measured, and tested as an element of UWB radar-based imaging system for non-invasive differential temperature measurement of muscle tissue.

Keywords: UWB, bow-tie, dipole, antenna, medical, imaging, confocal, radar, ultra-wideband, balun, tapered, hyperthermia, contactless, temperature, measurement

Abstrakt

Tato diplomová práce se zabývá návrhem širokopásmové antény pro mikrovlnné zobrazovací metody v medicíně. Je prezentován návrh planární motýlkové antény s planárním symetrizačním členem. Geometrie antény je optimalizována pomocí v simulátoru elektromagnetického pole, založeném na metodě konečných diferencí v prostoru a čase (FDTD). Anténa je vyrobena, měřena a testována jako element zobrazovacího systému na bázi UWB radaru pro neinvazivní měření teploty ve svalové tkáni.

Klíčová slova: UWB, bow-tie, dipól, anténa, lekářské aplikace, zobrazování, konfokální, radar, širokopásmový, balun, symetrizační člen, hypertermie, bezkontaktní, měření

Contents

List of Figures

Chapter 1

Introduction

Microwave imaging methods in medicine have been explored intensively in the last two decades as an alternative to currently used imaging methods. The possibility of their use has been investigated, among other things, for the detection of breast cancer [8], for the brain stroke detection [9] and for the non-contact temperature measurement [2].

The advantage of microwave imaging methods, compared to the imaging methods currently used in medicine (MRI, CT, PET, etc.), is their relatively small acquisition and operating costs. Another advantage is their simplicity and compactness, which makes it possible to use microwave imaging methods where the use of other imaging methods is impossible. An example of such applications is the detection of stroke in ambulance vehicles, or contactless measurement of a temperature of the patient's tissue, while hyperthermia treatment is applied. Medical harmlessness of microwave imaging methods is another factor that increases the interest in developing these methods.

Non-contact temperature measurement in the human body (using microwave imaging methods) is possible thanks to the dependence of permittivity and conductivity of tissues on temperature (further discussed in chapter 2). It can be achieved both by microwave tomography and radar-based imaging (confocal imaging). Microwave tomography includes methods, which are able to estimate the dielectric profile of the examined tissue. Radar-based imaging methods are able to locate dielectric inhomogeneities (scatterers) within a tissue, without the ability to reconstruct dielectric profile [7]. The advantage of radar-based methods is a usually smaller computational difficulty of reconstruction algorithms. A combination of both approaches is also possible and can be advantageous. Such example is reducing the analyzed area of tissue to area containing significant inhomogeneities by a radar-based method, which can effectively fasten computations of microwave tomography reconstructing algorithm - dielectric profile of the tissue is then reconstructed only in the previously limited area.

Confocal imaging is based on the detection of electromagnetic waves reflected (scattered) on the dielectric interfaces with different permittivity resp. electrical conductivity. Dielectric

inhomogeneities are localized using signals captured on measuring antennas, processed with beamforming algorithm. The basis of most of these algorithms is the delay-and-sum (DAS) algorithm, which is based on time shifting and summing of captured signals in particular focal points [7] . Detection principles are further discussed in chapter 2.

Transmitted signals used in Radar-based imaging methods in medicine are spread over ultra-wide frequency band (UWB radar) and so provide high resolution in the time domain, which is for most medical applications necessary. The transmitted signal differs with the radar system used. It can be formed by short periodically repeated pulses, pseudorandom binary sequence, etc. Alternatively, frequency domain measurement with a vector network analyzer (VNA) can be used to obtain s-parameters, which are then transformed from frequency into the time domain using Discrete Fourier Transform (DFT). This approach is described in more detail in chapter 2.

Antennas intended for the use in the UWB radar-based imaging system have to satisfy multiple performance demands in the supposed ultra-wide frequency band. These demands can be theoretically satisfied by only a few types of antennas, which are further discussed in chapter 4. From possible solutions, bow-tie dipole antenna was chosen to be designed, as it can satisfy the requirements of this work, and it' s fabrication is relatively simple. The geometry of this antenna was optimized using simulations in FDTD solver (see chapter 5). The antenna was fabricated (see chapter 6) and was used to build a UWB radar system for temperature detection in muscle tissue (the system is described in chapter 7). Performance of this UWB radar system was tested and the results are shown in chapter 8.

Chapter 2

Microwave imaging methods in medicine

Microwave imaging of biological tissues is possible, thanks to the existence of dielectric inhomogeneities within the analyzed region. On the interface of materials with different permittivity, resp. conductivity, an incident electromagnetic wave is reflected (scattered). Inhomogeneities (scatterers) may be of various origins. They can be divided into two groups, namely static and dynamic.

Dielectric properties of static scatterers do not change during the measurement procedures. Static scatterers are ever present in consequence of the inhomogeneous structure of the human body and tissues. However, some parts of the human body are relatively dielectrically homogeneous, allowing the presence of an unusual static scatterer to be detected. Such example is the detection of breast cancer, as tumorous tissue has significantly different dielectric properties than surrounding healthy breast tissue. The dielectric properties of the dynamic scatterers vary considerably between single measurements. If dynamic scatterers are to be investigated, the use of differential measurement is advantageous. Measurements made at an appropriate time interval are subtracted one of each other, which suppresses the static background (static inhomogeneities), and thus enables the detection of relatively small dynamic scatterers. Examples of differential measurement use in medical imaging are brain stroke detection or differential temperature monitoring. A brain stroke is characterized by a decrease or increase in blood volume in a particular part of the brain, causing a change in dielectric parameters in this area. Temperature monitoring is possible thanks change of dielectric properties of tissues with the temperature. The dependency of relative permittivity and specific conductivity of muscle tissue on frequency and temperature is further discussed in the following chapter 3.

Non-invasive temperature measurement in the human body (using microwave imaging methods) can be achieved both by microwave tomography and by UWB radar-based imaging

(confocal imaging). Microwave tomography is based on the measurement of perturbations of an electromagnetic field propagating through the tissue. Perturbations caused by an investigated object in the tissue are used to estimate object shape and dielectric properties. Microwave tomography usually requires more computational power than other (currently used) tomography based imaging methods (CT, PET, ultrasound tomography), as dimensions of the analyzed objects are comparable to the wavelength of electromagnetic wave, used for the tissue investigation. Significant computational demands imply a longer calculation time, which is a major disadvantage of microwave tomography compared to UWB radar imaging, where the computational requirements of the reconstructing algorithms are usually relatively low. In the situations where measurement time plays a significant role, which may be the case of dynamic scatterers investigation, UWB radar imaging methods may be more appropriate than microwave tomography methods.

2.1   UWB radar-based imaging

Imaging methods based on UWB Radar can locate dielectric inhomogeneities (scatterers) within a tissue, without the ability to reconstruct dielectric profile. In some applications, knowledge of dielectric profile is not necessary, which is the case of non-invasive temperature measurement during microwave hyperthermia. Analyzed tissue is irradiated by the transmitting antenna and (back)scattered electromagnetic energy is captured on the receiving antennas. Transmitting antenna is radiating microwave signal, being spread over an ultra-wide frequency band. Signal captured on m-th receiving antenna can be described by the following formula

$$x_m(t) = s_m(t) + n_{ms}(t) + n_{md}(t) \tag{2.1}$$

where x_m is captured signal on m-th antenna, s_m is signal component caused by scattering, n_{ms} is static clutter and n_{md} is dynamic clutter. Static clutter component is of much higher intensity than investigated signal (s_m), and thus has to be efficiently suppressed, so scatterers within analyzed tissue become observable [1].

Clutter signals contain both static and dynamic component. Static component, which is time-invariant, is caused mainly by crosstalk between transmitting and radiating antenna, by antenna reverberation and by reflections from patient's skin or other tissues covering analyzed region (e. g. cranium in brain stroke detection). Dynamic clutter is responsible for the variations of clutter signal among performed measurements unrelated to the change in the dielectric profile of analyzed tissue. Sources of dynamic clutter can be both internal e. g. drift effects caused by small temperature changes of antennas [1]) and external (electromagnetic interference).

By using differential measurement, static clutter is sufficiently suppressed by subtraction

4

of measured signals. Dynamic clutter is not easily subtractable but can be minimized by averaging of several consecutive measurements. Differential signal Δx_m obtained from non-averaged pair of measured signals (x_{m1}, x_{m2}) can be described by following formula

$$
\begin{aligned}
\Delta x_m(t) &= x_{m1}(t) - x_{m2}(t) \\
\Delta x_m(t) &= s_{m1}(t) + n_{ms1} + n_{md1}(t) - s_{m1}(t) - n_{ms1} - n_{md1}(t) \\
\Delta x_m(t) &= \Delta s_m(t) + \Delta n_{md}(t)
\end{aligned}
\tag{2.2}
$$

where Δs_m is a differential component caused by scattering and Δn_{md} is differential dynamic clutter. Differential signals Δx_m are thus calculated for every irradiation scenario (for each transmitting and receiving antenna position). If all antennas have fixed position (multi-static array) and are used both as transmitting (in their turn) and receiving (in other antenna turn), $N(N-1)$ differential signals are obtained (N is the number of measuring antennas). If VNA is used as a UWB radar (as described later in this chapter) the number of obtained differential rises to $N \cdot N$ as transmitting antenna is also receiving at the same time. If reciprocal signals are omitted (as they won't provide any additional information) the number of signals to be analyzed is halved to $N(N+1)/2$.

These differential signals are then processed by beamformer algorithm, to obtain a reconstruction of the scattering profile of the analyzed region. Most of these beamformer algorithms are modifications of the delay-and-sum (DAS) algorithm, which is based on the time shifting and summing of captured signals in the focal points [7]. Time-shift $T_{(d_m)}$ for each captured signal and each focal point r_0 is calculated by estimating propagation speed v_p of the electromagnetic wave in measured tissue with dielectric constant ε_r, and from known round-trip distance d_m between transmit antenna, particular investigated focal point and receiving antenna (equation 2.4).

$$
T(d_m) = \frac{d_m}{v_p} \quad , \quad v = \frac{c}{\sqrt{\varepsilon_r}}
\tag{2.3}
$$

Scattered energy from focal point is then summed and squared. By doing this procedure across all focal points, 2D resp. 3D energy profile is created. Intensity $I(r_0)$ in particular focal point r_0 is obtained from the following formula (originally presented by Nilavan R. et al. in [37])

$$
I(r_0) = \sum_{t=-T_W/2}^{T_W/2} \sum_{m=1}^{N(N+1)/2} \left(w_m(d_m) \cdot \Delta x_m\big(t + T(d_m)\big) \right)^2
\tag{2.4}
$$

where T_W is predefined time-window and w_m is a weighting factor to compensate for path-dependent attenuation. This multi-static version of the DAS algorithm was used to create reconstructions of dielectric profile presented in the chapter 8. Please notice, that presented formula is adapted to discrete-time signals, obtained by transformation of s-parameters to time domain as described in the following section.

2.2 Vector network analyzer used as UWB radar

Vector network analyzer (VNA) can be used with the application of Inverse Discrete Fourier Transform (IDFT) to measure reflections in the time domain. This makes possible to use VNA with proper antennas connected as radar for near field applications. Measured s-parameters are transformed into the time domain, thereby obtaining impulse responses. Due to limited frequency band measured, step change appears in the frequency domain at the first and the last frequency point. A step change in frequency domain causes ringing-type distortion (formation of side peaks next to main signal peak) in the time domain when IDFT is applied, which can cause masking of minor scatterers, and worsen the resolution. Level of side peaks (ringing distortion) can be suppressed by frequency windowing of measured s-parameter data. Side effects of frequency windowing are signal peak widening and dynamic range limiting [36]. The ratio between these effects (side peaks level suppression vs. side effects) depends on the type of window used. Influence of frequency windowing is shown in fig. 1. The figure shows impulse responses obtained by transformation of s_{11} parameter of an open-ended coaxial cable into time domain depending on frequency windowing used.

VNA frequency domain measurement of s-parameters should be properly set, so transformed time domain signals will meet the requirements for sufficient resolution and alias free time range. The relation between frequency and time domain (in means of frequency domain measurement setup) is described by following formulas

$$\Delta t = \frac{1}{f_{BW}} = \frac{1}{\Delta_f \cdot N_f} \quad , \quad t_{alias} = \frac{1}{\Delta_f} \tag{2.5}$$

where Δt is impulse response time-step, f_{BW} is frequency band measured, Δ_f is frequency step, N_f number of measured frequency points and t_{alias} is alias free time range. This approach was applied to obtain time-domain signals x_m used for the reconstruction of the scattering profile of the phantom under test as described later in chapter 8.
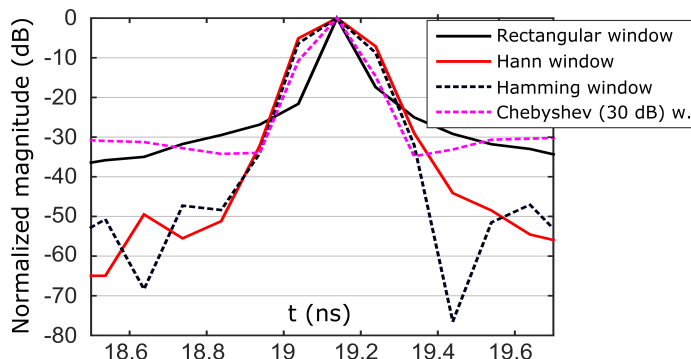

Fig. 1: Frequency windowing effect on relative impulse response magnitude of coaxial open-ended cable (N-type male connector).

Chapter 3

Dielectric properties of biological tissue

Non-invasive temperature measurement via UWB radar is possible, due to the existence of dielectric contrast between tissues with different temperature. In microwave hyperthermia treatment, the tissue is being heated up to the maximum temperature of 45° C, and thus, the maximum possible temperature difference relative to the normal human body temperature is about 8° C. Dielectric properties of biological tissues can be described on the single frequency with relative complex permittivity [6] as follows

$$\varepsilon^* = \varepsilon^, - j\varepsilon^" = \varepsilon_r - j\frac{\sigma}{\omega\varepsilon_0} \tag{3.1}$$

where ε^* is complex relative permittivity, $\varepsilon^,$ is real part of ε^* and equals to relative permittivity ε_r, $\varepsilon^"$ is imaginary part of ε^*, ω is angular frequency, σ is specific conductivity and ε_0 permittivity of vacuum. The imaginary part of relative complex permittivity is responsible for losses in a dielectric material and represents out of phase component of oscillations of electrical dipoles in biological tissue [6]. Both relative permittivity and specific conductivity are scalars, as biological tissues are usually treated as isotropic materials. Specific conductivity and loss tangent can be expressed from complex permittivity as follows

$$\sigma = -\omega\varepsilon_0\text{Im}(\varepsilon^*) \quad , \quad \tan\delta = \frac{\varepsilon^"}{\varepsilon^,} = \frac{\delta}{\omega\varepsilon_0\varepsilon_r} \tag{3.2}$$

The complex relative permittivity of human tissues is temperature dependent, and besides frequency dependency of its imaginary part, which follows from definition 3.2, it exhibits additional frequency dependency and thus, it is a dispersion material. Two-pole Cole-Cole model based on measurements of dielectric parameters of porcine muscle tissue is presented by S. Ley in [5]. This model is valid in the frequency range from 0.5 GHz up to 7 GHz and the temperature range from 30°C up to 50°C. Ley's model shows significant dependency of complex permittivity of muscle on temperature along with strong dispersive behavior. Change

of relative permittivity with temperature is most distinctive on the frequency of around 1 GHz and fades on the frequency of around 6 GHz as shown in fig. 2 and 3. Weak dependence of permittivity on temperature above the frequency of 4 GHz along with frequency dependent attenuation of backscattered electromagnetic waves (as reported in [3]) are main factors that limit the maximum usable frequency of UWB radar-based imaging systems intended for temperature detection in biological tissues.
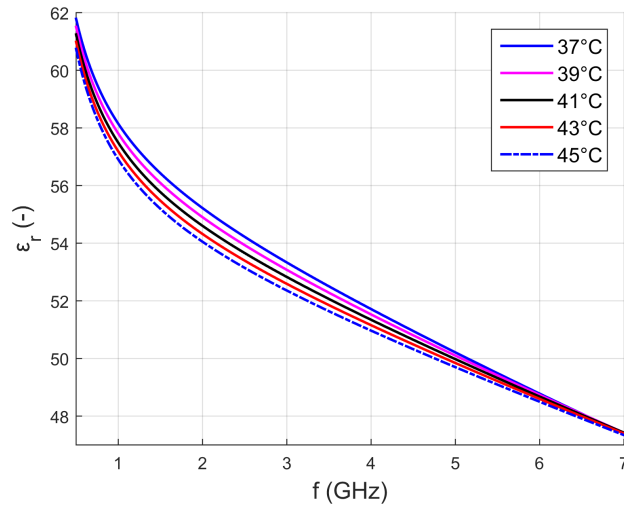

Fig. 2: The estimated relative permittivity of muscle tissue over the frequency range 0.5 - 7 GHz and temperature range 37° C - 45° C. Model adopted from [5].
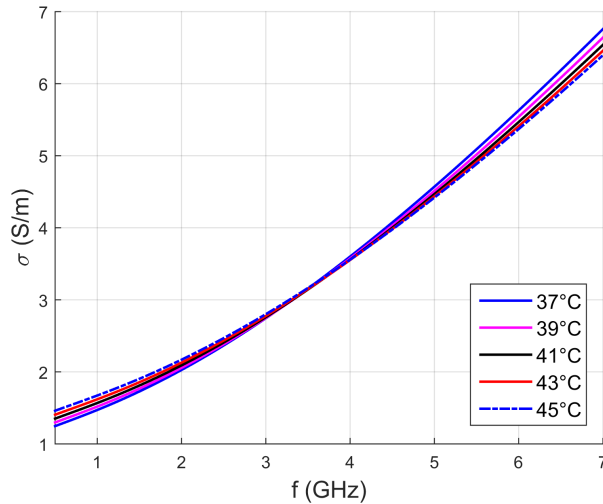

Fig. 3: The estimated specific conductivity of muscle tissue over the frequency range 0.5 - 7 GHz and the temperature range 37° C - 45° C. Model adopted from [5].

Chapter 4

Antennas for UWB radar-based imaging

Antennas intended for the use in the UWB radar-based imaging system have to satisfy multiple performance demands in the supposed ultra-wide frequency band. The most important of them, at least according to [16] and [17], are:

- Efficient transmission of electromagnetic energy into the tissue, which is associated with a low return loss of the antenna, small losses in antenna circuit and low energy radiation outside the analyzed tissue.

- Suitable (near field) radiation patterns, as in 3D UWB medical imaging systems are usually required wide beamwidth in the azimuth plane and acceptably narrow beamwidth in the elevation plane.

- Proper impulse characteristics of the antenna (minimal distortion in the time domain), as for the high spatial resolution of the UWB imaging system, short impulse response resp. acceptably small ringing in the time domain is required.

- Angle dependency of the impulse response (fidelity) should be ideally small, as backscattered signals arrive from different directions.

- Acceptable physical dimensions of the antenna, which allow building antenna array with the required spacing of the antennas.

- Constant performance of the antenna over supposed ultra-wide frequency band.

Satisfying all of these demands in one antenna design is hardly achievable. Different types of UWB antennas offer different performance and satisfaction of those demands. Starting from the demand for constant performance of the antenna in the ultra-wide frequency band, the choice of antenna type will narrow to three groups of antennas [18]:

- Variations of dipole resp. monopole antennas, usually derived from a biconical antenna.

- Antennas with curved geometries or with absorptive loading.

- "Frequency independent" antennas (most commonly spiral antennas and log. Periodic dipole arrays).

As already mentioned, the application of UWB radar requires minimal distortion in the time domain. To minimalize distortion, the antenna should have constant radiated fields over the frequency, and also the variation of the phase of the radiated fields with frequency should be linear. Distortion of the signal by means of a non-linear varying phase of radiated fields is the reason, why are frequency independent antennas (spiral, etc.) not suitable for UWB radar applications. Their phase center varies with frequency, which causes dispersive behavior of antenna, and thus distortion of the pulse in the time domain.

The rest two categories of antennas geometries cover field of the UWB medical imaging systems. Commonly used antennas in this field are Vivaldi planar antenna eg [19], horn resp. ridged horn antennas eg [20], [21], planar monopoles eg [22], [23] and finally Bow-tie dipoles and its modifications eg [24], [16], [25].

Planar Vivaldi antennas use exponencially tapered antipodal arms to radiate energy into the tissue. The biggest advantages of this design are an extremely wideband performance and good efficiency of radiation (minimum backward radiation). As shorter wavelengths are radiated at the beginning of the taper, and conversely longer wavelengths near the end of the taper, Vivaldi antenna need to be placed in matching medium, so energy can be effectively transmitted to analyzed tissue. Burqui, author of balanced antipodal Vivaldi antenna design [19], used as matching medium canola oil, which has a permitivity of $\varepsilon_r = 2.5$ and corresponds to the permittivity of substrates used for fabrication of antenna (with ε_r slightly higher). Canola oil can be used as a matching medium for breast imaging (the approximate permittivity of breast tissue is $\varepsilon_r = 6$). The aim of this work is to design an antenna, which will be used in the analysis of the muscle tissue, which has permittivity of around $\varepsilon_r = 50$. As matching liquid for such application, purified water with permittivity of around $\varepsilon_r = 80$ is usually used. Such high permittivity dielectric surroundings near vivaldi antenna structure significantly affect antenna radiation and can cause energy radiation in unwanted directions, and thus degradation of radiation effectivity. Also, vivaldi antenna has not negligible height, which makes use of this antenna as an array element difficult in imaging applications below 2 GHz.

Horn resp. ridged horn antennas biggest advantage among others is good radiation efficiency, as backward and side radiation of electromagnetic energy is highly suppressed. Similarly, as with Vivaldi antenna, the matching medium has to be used to fill horn in a considered application. Possible materials are already mentioned water and also ceramics with the per-

mittivity of around $\varepsilon_r = 60$, which was used by Clemente in his horn design [20]. High permittivity dielectric inside the horn antenna significantly reduces physical dimensions of antenna, which makes it possible to use in medical imaging applications. In the same time, high permittivity fill reduces dimensions of feeding area (coaxial probe transition), which together with ceramics dielectric fill makes design and fabrication of such antenna relatively complicated.

Planar monopole antennas as Jafaris UWB monopole [22] offer a low-cost solution to the problem, as they are easy to fabricate. Planar monopoles do not need matching liquid, as they can be placed on the surface of the analyzed tissue. Monopole antennas can be fed directly by unsymmetrical feeding, which makes a design of monopole much easier, since UWB balun is not needed. However, the advantage of the simplicity of planar design entails the drawback of power supply in the plane of the monopole patch, which is not very appropriate and makes use of such monopole as array element difficult. Furthermore, radiation pattern varies not negligibly with frequency [23], which, as explained before, may cause distortion in the time domain.

Bowtie dipoles, generally planar dipoles or its modifications can be seen as a compromise design in means of design and fabrication difficulty. Since basic bowtie geometry is very simple, and (fed with ideal discrete 50 Ω voltage source in feed point) such geometry is very broadband, design of such antenna reduces primarily on the design of a feeding circuit with a proper broadband balun. Balun transforms unbalanced input (usually SMA coaxial connector) to balanced output as a dipole is a symmetrical structure, and thus requires symmetrical feeding. In comparison with horn or vivaldi antenna, bowtie has less radiation effectivity and is more sensitive to the surrounding environment as more energy is radiated outside the analyzed tissue (due to dipole radiation pattern). However, due to the high permittivity of the muscle tissue, the greater part of the electromagnetic energy emitted by the dipole is concentrated into the phantom, and thus the efficiency drop due to radiation outside the phantom half-space is not so pronounced. Moreover, a planar dipole can be attached right to the tissue surface, so there are no additional losses in the medium between the antenna and the tissue and furthermore, matching liquid is not necessary, which facilitates the practical application of such a UWB imaging system. This work deals with bowtie type antenna design, as it seems to be a suitable choice for the application under consideration.

Chapter 5

UWB bow-tie antenna design

The procedure of the UWB bow-tie antenna design can be divided into three main parts. First is the design of bow-tie arms shape, the second part deals with a UWB balun design, as a dipole is symmetrical structure, and requires balanced feeding, and the third part finally optimizes the geometry of the whole antenna to meet given requirements on performance.

5.1 Design of bow-tie arm's shape

As bow-tie antenna is planar structure usually designed as one layer PCB, design of bowtie arms is simplified to the optimization of 2D bowtie arms shape. Influence of different arm geometries of bow-tie antenna's arms on bow-tie performance was examined in detail in [26]. In mentioned paper authors show the effect of bow-tie geometry on antenna impedance matching and antenna gain. As modifications of bow-tie geometry can enhance antenna performance and also miniaturize bow-tie dimensions, some of promising arms shape modifications presented in [26] were chosen to be compared. These geometries, namely "REBA" (rounded bow-tie antenna), "TBARC" (triangle bow-tie antenna with rounded corners) and "TBA" (triangle bow-tie antenna) are shown in fig. 4. Models of bow-tie antennas were made and their s_{11} parameter (related to 50 Ω feeder) was simulated. All simulated shapes are derived from classical bow-tie shape with a total length of 30 mm, width 30 mm and thus with dipole arm angle $\theta = 45°$ (see fig. 4.). Bow-tie surface was directly attached to homogenous phantom with dielectric parameters corresponding to muscle tissue ($\varepsilon_r = 53$, $\sigma = 1.2$). Bow-tie arms were placed on the substrate of height h = 1.524 mm with dielectric parameters corresponding to Rogers RO4003C. Results of simulation are presented in fig. 5. Obtained s_{11} curves show, that TBAs are better impedance matched on frequencies below 1 GHz, which is a logical consequence of the overall reduction of the antenna size on rounded bow-tie modifications. On the other hand, all of the simulated shapes have sufficient impedance matching ($s_{11} < $ -10 dB) above 1 GHz. As a small physical size of the antenna is in medical imaging advantage,

TBARC geometry with a rounding radius of 6 mm was chosen for the proposed antenna. This geometry enables reducing of bow-tie width from 30 mm in classical TBA geometry to 13 mm in TBARC.

Bow-tie impedance is also influenced by dipole arm angle θ. In simplified terms, radiation resistance is rising with decreasing θ (decreasing arm's width) and conversely radiation resistance is decreasing with rising θ (increasing arm's width). Also, by increasing θ angle, the reactance of dipole is decreasing (capacitive character) and conversely by decreasing θ angle, the reactance of dipole is increasing (inductive character). In this work θ was fixed to 45° as a whole antenna structure with balun showed the best impedance matching with $\theta = 45°$.
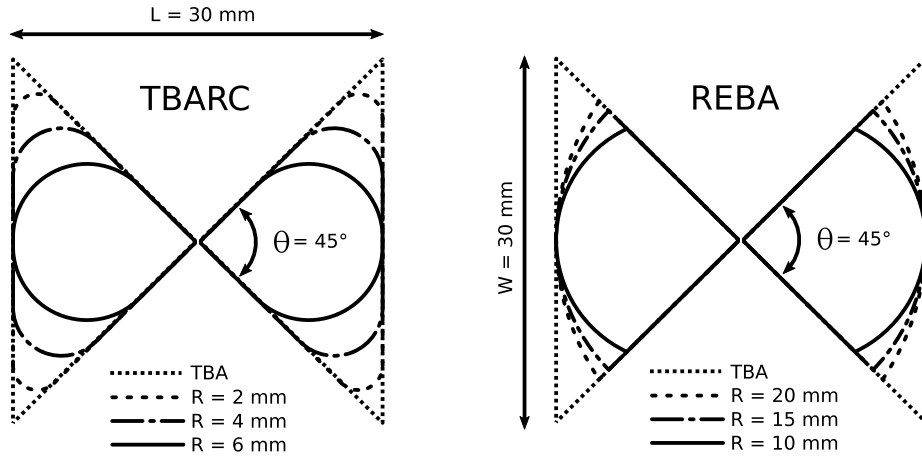

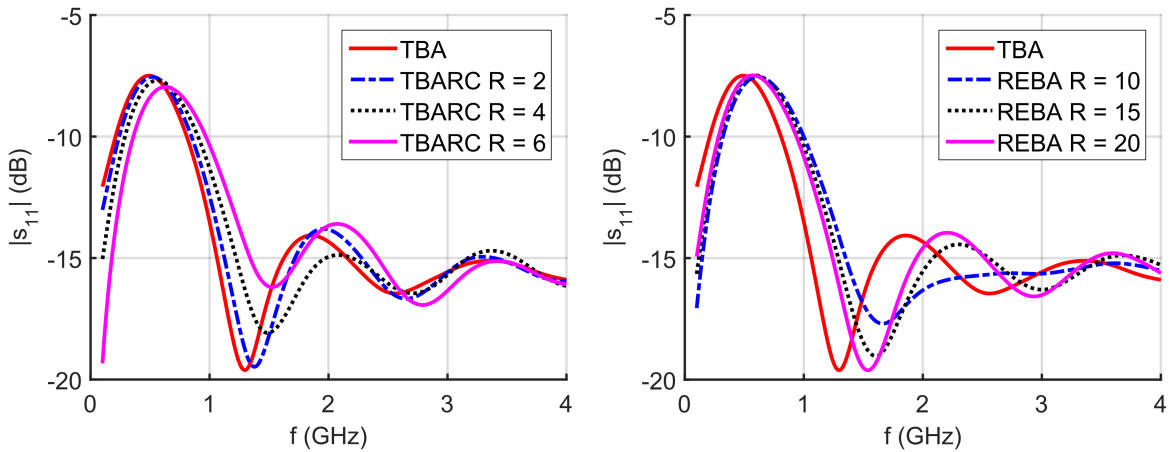Fig. 4: Modifications of bow-tie arms shapes derived from the basic shape of TBA.

Fig. 5: Module of s_{11} parameter of simulated bow-tie antennas of different arms shapes with TBARC geometry on the left and REBA geometry on the right.

13

5.2 UWB balun design

UWB balun is a key feature in the design of symmetrical UWB antenna. Balun (BALanced to UNbalanced) is symmetrization circuit to transfer unbalanced line (unsymmetrical) to balanced line (symmetrical). A symmetrical line can be defined by the existence of geometrical (electrical) axis of symmetry (virtual ground). Examples of such symmetrical lines are a two-wire line, coplanar strips, coplanar waveguide, double side parallel stripline (DSPSL) or symmetrical microstrip line. Most of the symmetrical lines are unshielded, and thus radiate, and are prone to conductive objects in their vicinity, and also to external electromagnetic interference, which negatively affects their performance. For these reasons, larger distances between transceiver resp. reciever and antenna are bridged by shielded unsymmetrical line (in microwave imaging applications usually coaxial line). If the proposed antenna requires symmetrical feeding, proper symmetrization circuit should be then added to transform between the unbalanced output of the feeding line and balanced input of the antenna.

Most of the classic narrowband antenna baluns are based on the line sections of the lengths $\lambda/4$ resp. $\lambda/2$ and their characteristic behavior. This approach of balun design can be hardly used in the UWB application requiring bandwidth ratio 2:1 and higher, since characteristic behavior of these line sections is based on their electrical length, which is, in such wide frequency band, changing rapidly. Broadband baluns are therefore based on different physical principles. In the proposed frequency band (1-3 GHz) are most of the balun designs based on one of the two mutually different approaches. First of them uses a gradual, step or other particularly-shaped transition between unbalanced and balanced line ("cutaway" or "tapered" transition baluns). Such baluns are usually designed as planar structures but were already designed also in coaxial geometry [27]. The second approach utilizes symmetrization with coils wound on toroidal or bar ferrite cores.

Tapered baluns can provide symmetrization in an ultra-wide frequency band, and can work up to tens of GHz [28], [29], and their design (especially planar) is relatively simple. Most of the planar balun designs with impedance transformation from 1:1 up to 1:2 use transition between the microstrip line and double-sided parallel strip line (ML to DSPSL balun), although baluns based on different transitions were also studied and designed [30],[31]. Performance of ML to DSPSL balun is defined by the shape of ground transition (although additional modifications are possible eg [29]). Comparison of step, linear-shaped and rounded transition between microstrip and DSPSL is provided in [28]. Another commonly used transition ground shape is exponential [19]. Transition shape was further optimized in [32] resulting in more complex shaped transitions. Although the performance of such optimized transitions can be superior, according to previously mentioned papers, less complex ground transition geometries should still provide sufficient performance in the proposed frequency band. The disadvantage of tapered baluns is their not-negligible length, as the minimum length of tapered part of

such balun is recommended as $\lambda_g/4$ [29], where the guided wavelength is related to the lowest frequency in the proposed band. Beneficial review of not-only cutaway type UWB baluns is given in [33].

Small dimensions and ease of use are the biggest advantage od ferrite baluns. Such baluns can provide symmetrization from units of MHz to units of GHz. The disadvantage of ferrite baluns, despite limited frequency range, is especially low maximum RF power, that can be transformed. Another disadvantage over tapered (line-transition) balun approach is the fact, that accurate modeling of ferrite transformers in commercial electromagnetic field simulators is complicated, making it difficult to optimize the antenna structure with such a balun. Examples of usable RF transformer baluns are TCM1-83X+ from Minicircuits, with operation band 10 MHz to 8 GHz, maximum RF power 0.2 W and footprint approx 4 mm^2 and RFXF9503 from MiniRF with operation band 3 MHz to 3 GHz, maximum RF power 2 W and footprint also approx 4 mm^2.

5.3 Planar tapered UWB balun design

One of the advantages of bow-tie dipole type medical imaging antenna is the possibility to attach a dipole surface directly to the measured tissue. If this option is to be maintained then it is advisable to feed the bow-tie dipole in a direction perpendicular to the plane of the dipole arms, so that the power line does not constitute an obstacle to the dipole being applied to the tissue. Such feeding is also beneficial when an antenna is supposed to be used in an array, where its elements (antennas) are placed side by side. Tapered balun based on the transition from microstrip line to DSPSL can provide such feeding, as DSPSL can be designed easily with the characteristic impedance of 50 Ω, which is a suitable value for impedance matching of the bowtie dipole in an ultra-wide frequency band. Further, the difference between the width of microstrip active line and DSPSL line is relatively small (DSPS line of same characteristic impedance is about 30 % wider), which points on good compatibility of these microwave lines.

The characteristic impedance of DSPSL (Z_{DL}) can be calculated with formulas presented in [34]. However, an approximate value of Z_{DL} can be also easily obtained using known formulas for calculation of characteristic impedance of the microstrip line (Z_{ML}). Due to the existence of a virtual ground between parallel strips, Z_{DL} can be calculated as a doubled value of Z_{ML} calculated for a substrate of half height. This approach is derived in [35].

Strip widths of microstrip line (w_{ML}) and DSPSL (w_{DL}) were calculated to obtain 50 Ω characteristic impedance on Rogers RO4003C low loss substrate of height 0.508 mm. Length of balun was set to 48 mm being approximate $\lambda_g/4$ on 1 GHz. Different shapes of baluns were modeled as mirror pairs with microstrip line on both ends, and their s-parameters were simulated using FDTD based 3D electromagnetic field solver. The geometry of four proposed

baluns is shown in the fig. 6. Following results were calculated for the width of microstrip ground plane w_G=25 mm. Influence of w_G on transmission s-parameters of baluns was tested and is not significant. Results of simulations presented in the fig. 7 and fig. 7 show, that the best balun performance is achieved with exponential ground transition, which was adopted from [19]. Such balun has a module of s_{11} under -14 dB and module of s_{21} higher than -1.3 dB in the whole simulated frequency band. Further, a ripple of s_{21} module is smaller from all simulated baluns.
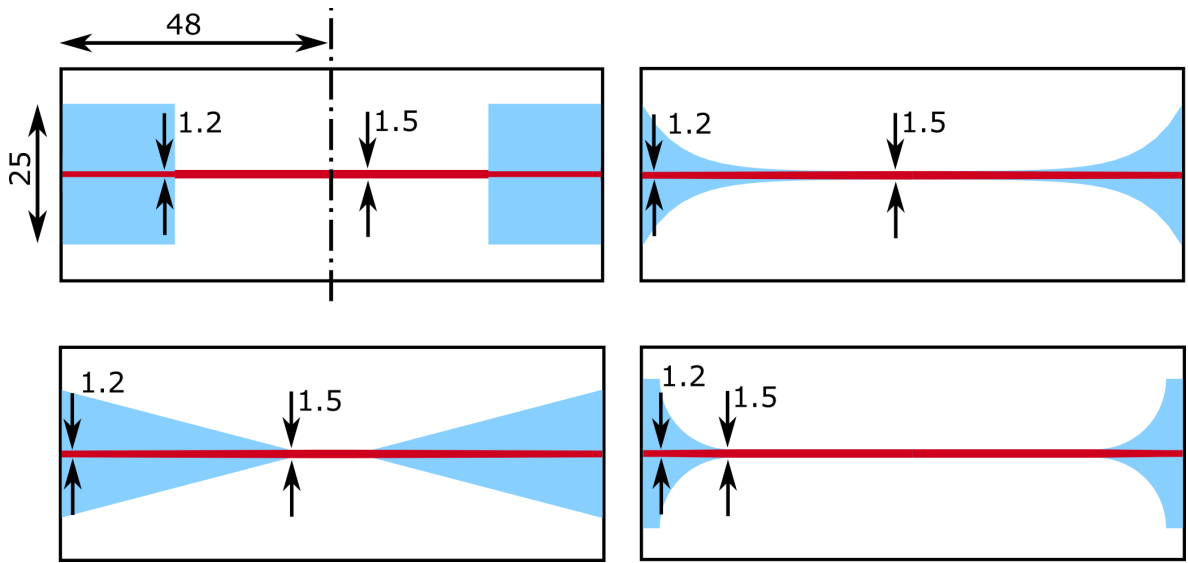

Fig. 6: ML to DSPSL to ML transitions geometries with different shapes of ground transition. All dimensions are in millimeters.
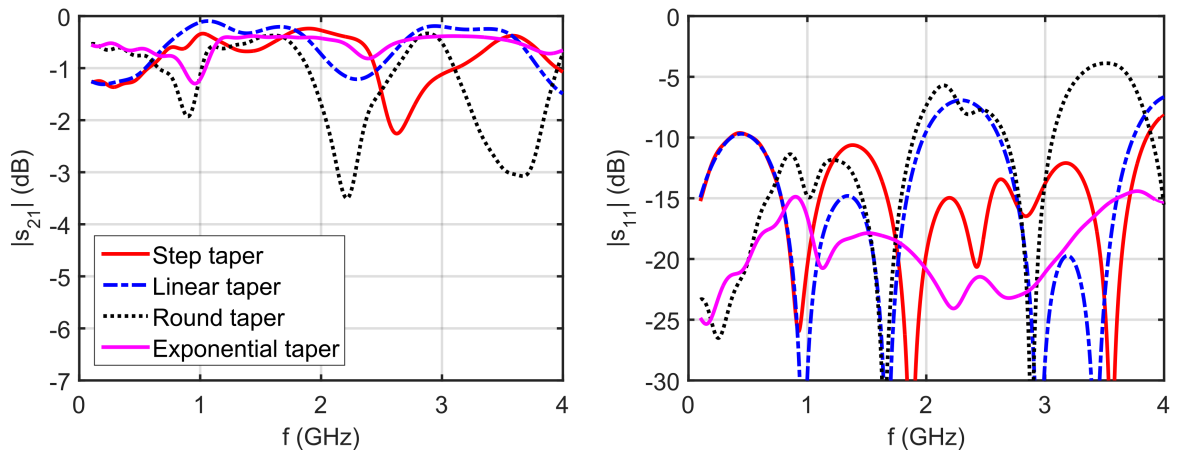

Fig. 7: The simulated module of transmission s-parameters of ML to DSPSL to ML transitions of different ground transition shapes.

16

5.4 UWB tapered balun-fed antenna design

Next step in the UWB bow-tie dipole design was connecting the designed UWB tapered balun to the dipole arms. Model of such antenna structure was made and s_{11} parameter was simulated for different widths of DSPSL strips w_{DL} to verification impedance matching between calculated 50 Ω DSPSL line end and bow-tie dipole. Model of the antenna is shown in the fig. 8. Since the geometry of the bow-tie feed point significantly affects input impedance of the bow-tie dipole (especially on the frequencies above 2.5 GHz) solder model was added to the feeding points, where DSPSL is connected to the bow-tie arms. Bow-tie arms were again attached to the model of homogenous muscle phantom ($\varepsilon_r = 53$, $\sigma = 1.2$) and supposed to be placed on Rogers RO4003C substrate. Results are shown in the fig. 9. Resulting s_{11} parameters magnitude show, that best impedance matching is provided with the DSPSL strip width $w_{DL} = 1.5$ mm. In the frequency band from 0.5 GHz up to 3 GHz, the magnitude of s_{11} of the antenna is under -10 dB.
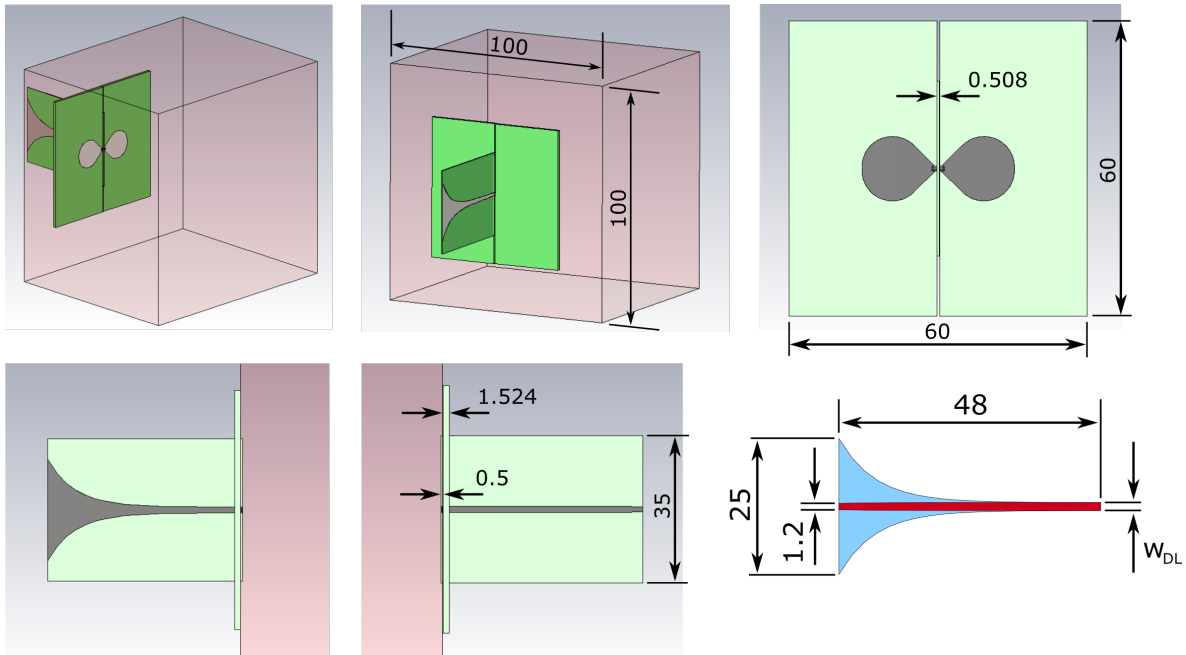

Fig. 8: A model of the balun-fed antenna attached to the homogenous muscle phantom. On the bottom right is a schematic picture of the conductive strips of the UWB balun. All dimensions are in millimeters.
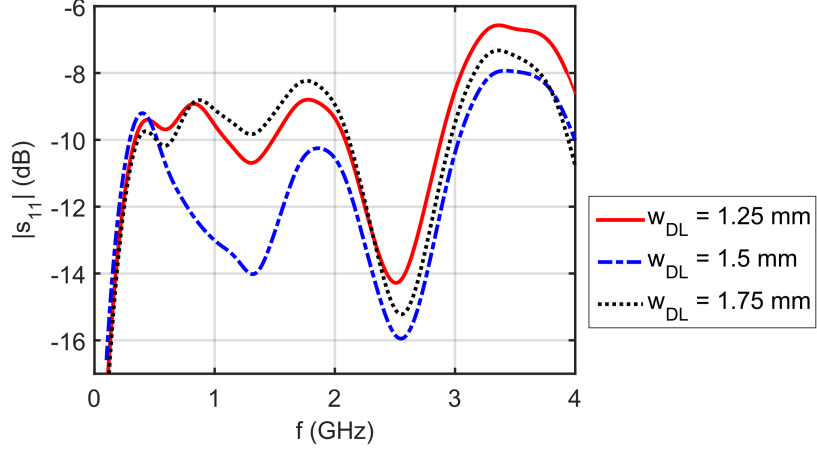
Fig. 9: The magnitude of s_{11} obtained by simulation of the UWB antenna with various DSPSL strip widths w_{DL}.

Although simulations showed that designed antenna can meet the demands of this work (magnitude of $s_{11} <$ -10 dB in the frequency band 1 GHz up to 3 GHz), the structure was further modified, to achieve better impedance matching in a proposed frequency band. Since rising dimensions of conductors in feeding points negatively affect impedance matching of the antenna, the additional taper was introduced to provide small width of DSPSL strips at the feeding point (1 mm). Further, width w_{DL} of DSPSL in distance L_P from feeding points were optimized. Balun modification is shown in fig. 10. Model of the UWB antenna with modified balun shape was again simulated to obtain s_{11} parameters for different widths w_{DL} and lengths L_P. Results are shown in fig. 11. Resulting modules of s_{11} parameter show, that introduced modifications of balun led to impedance matching improvement of the antenna in the whole simulated frequency band. Best impedance matching was achieved with modified baluns with $L_P = 2.5$ mm and $L_P = 4.5$ mm and widths w_{DL} around 2.3 mm. The simulated magnitude of s_{11} was in this setup under -15 dB from 0.8 up to 3 GHz and under -10 dB from 0.6 up to 4 GHz, which was the highest simulated frequency. For the fabrication of the UWB antenna, modified balun with $w_{DL} = 2.3$ mm and $L_P = 4.5$ mm was chosen.
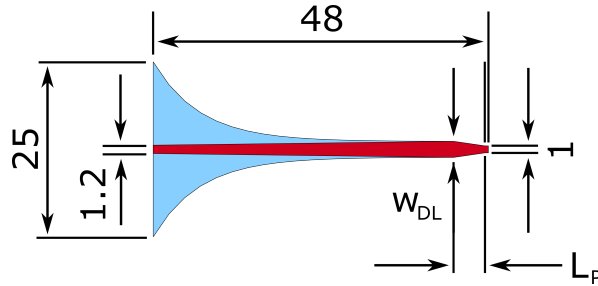

Fig. 10: A modified balun shape to provide better impedance matching with bow-tie dipole.
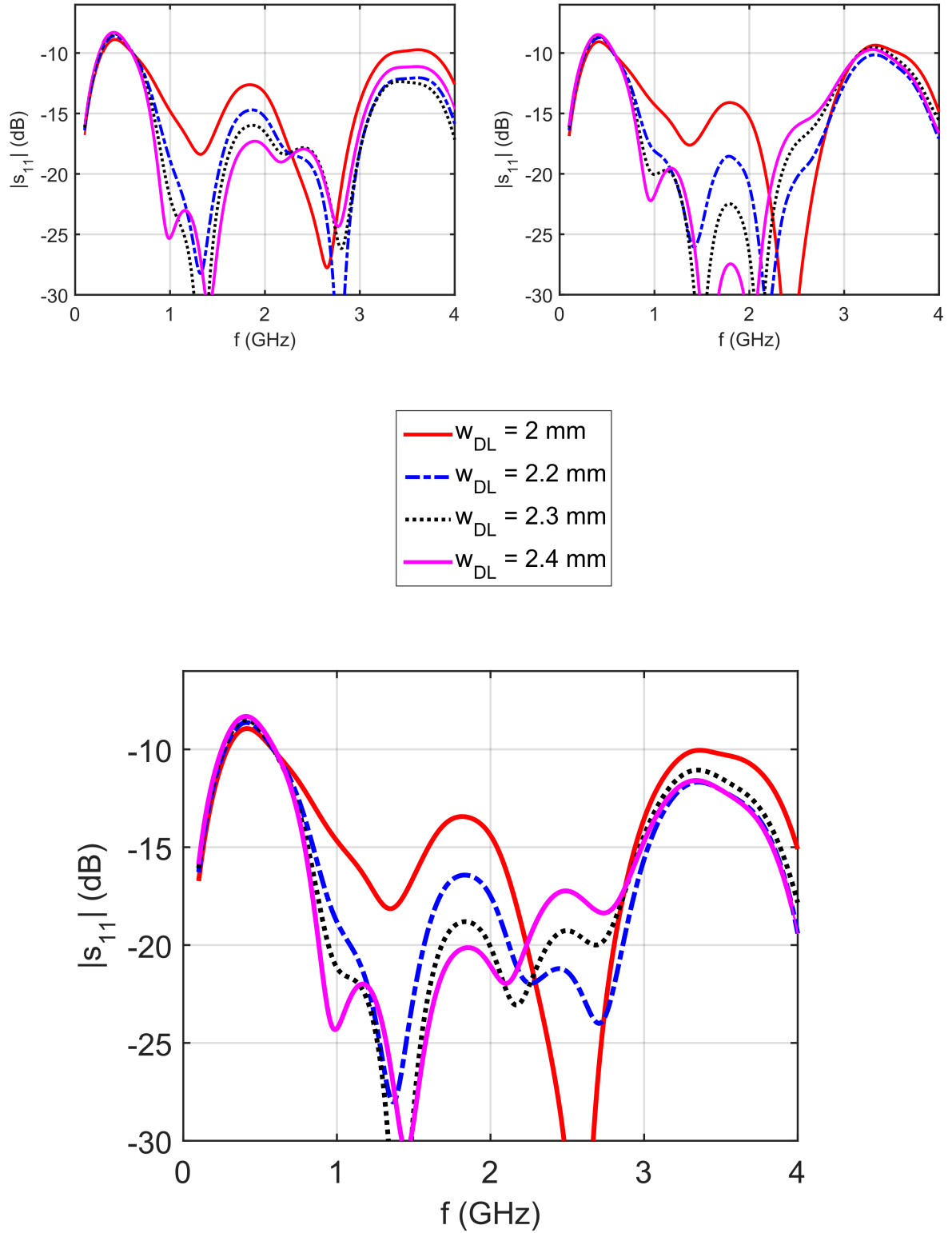
18

Fig. 11: The simulated magnitude of s_{11} of the UWB antenna with modified balun transition with $L_P = 2.5$ mm (top left), $L_P = 6.5$ mm (top right) and $L_P = 4.5$ mm (bottom). Results are plotted for various DSPSL strip widths w_{DL}.

19

5.5 Simulation of SAR distribution in homogenous phantom

SAR distribution in homogenous phantom exposed to microwave radiation from designed bow-tie antenna was simulated for showing directional characteristics of the antenna near field in the phantom half-space. SAR was simulated in the same setup as a module of s_{11} parameter in the previous chapter. Resulting SAR distribution is shown in Fig. 13 and Fig. 14 using azimuth and elevation cuts of the phantom (for clarity, the geometry of these cuts is specified in Fig. 12). Resulting SAR slices show that directional behavior of designed antenna is relatively stable, especially in the azimuth plane. Beamwidth in the elevation plane tends to increase with frequency, and also moderate ripple of beam shape appears on frequencies above 1.5 GHz.
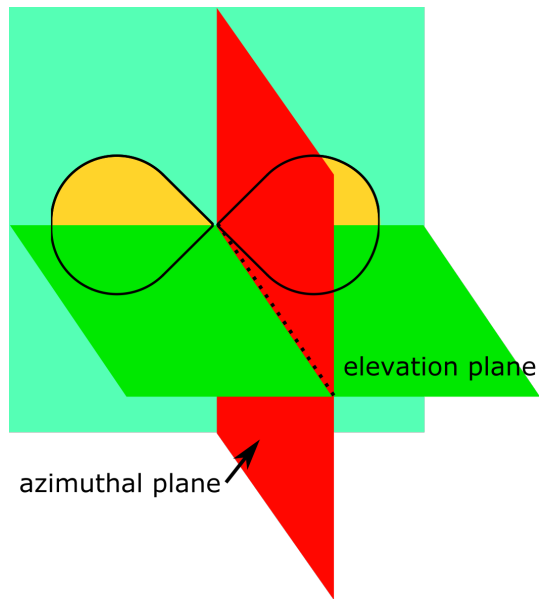

Fig. 12: Azimuth and elevation cuts, orientation relative to bow-tie antenna.
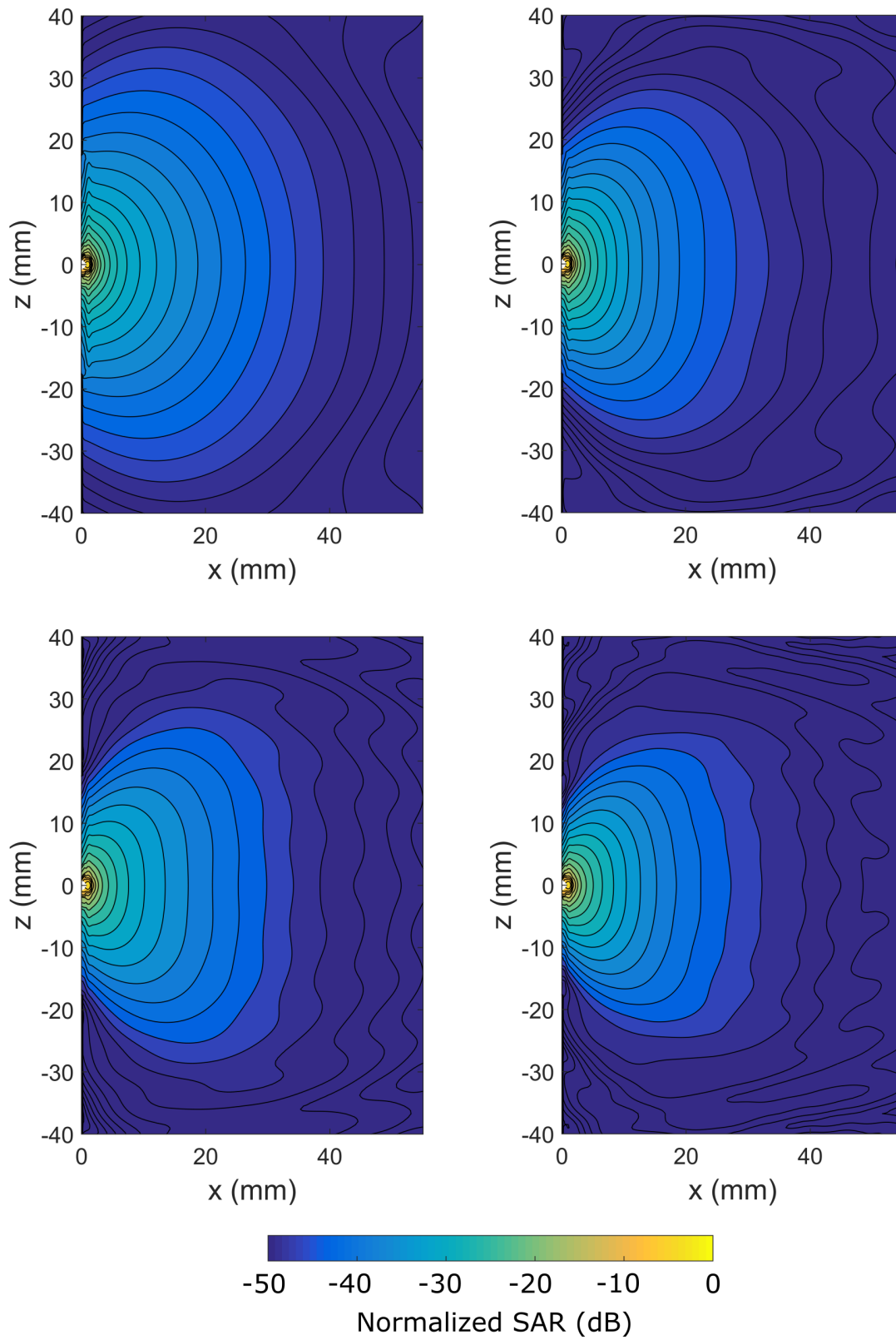
Fig. 13: Simulated distribution of SAR in the homogeneous phantom in azimuth plane cuts for different radiated frequencies. Top left 1 GHz, top right 2 GHz, bottom left 3 GHz and bottom right 4 GHz.
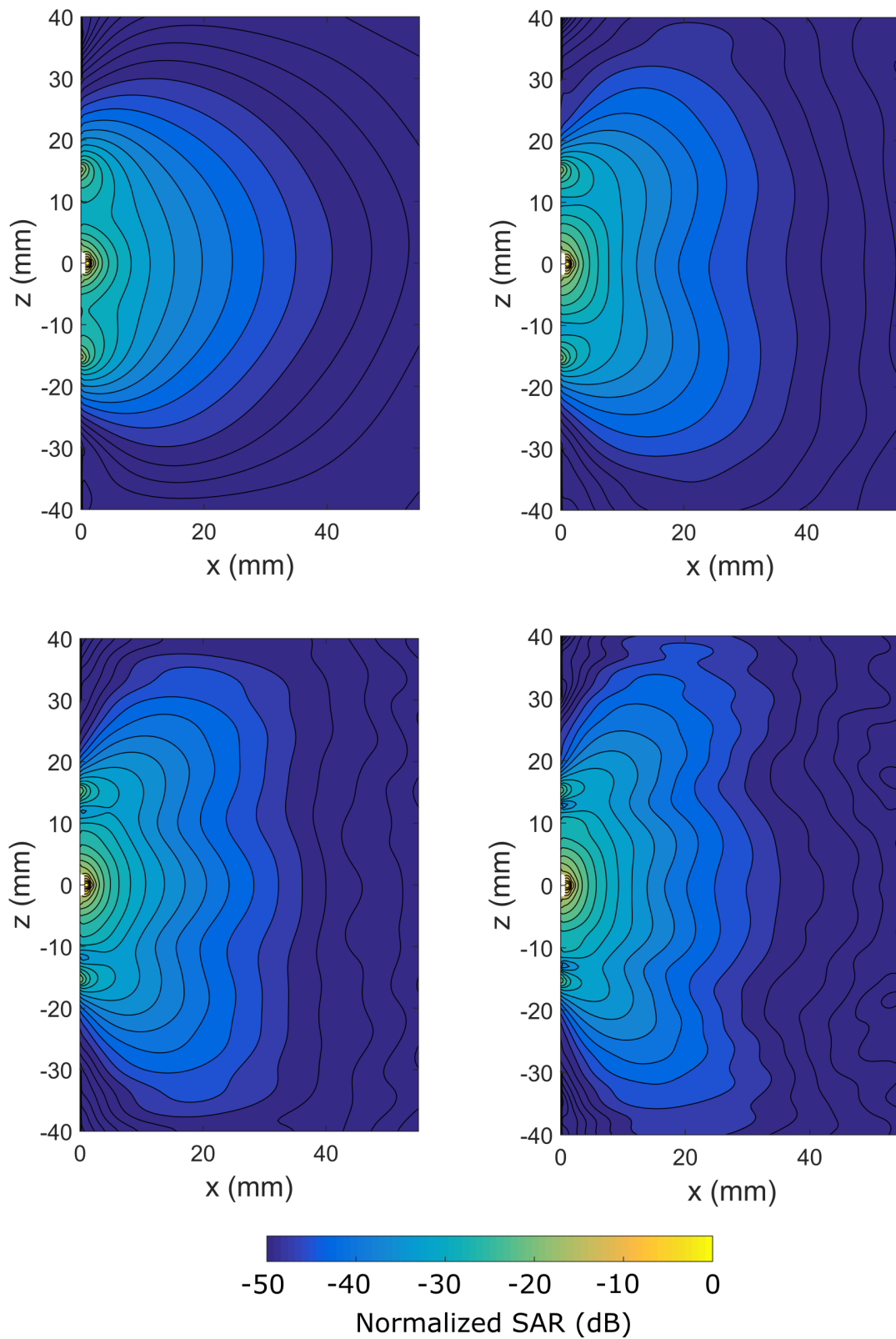
21

Fig. 14: Simulated distribution of SAR in the homogeneous phantom in elevation plane cuts for different radiated frequencies. Top left 1 GHz, top right 2 GHz, bottom left 3 GHz and bottom right 4 GHz.

22

5.6 Simulation of antenna capability to detect heated sphere

Antenna capability to detect dielectric inhomogeneity was simulated on the model of homogenous muscle phantom with an inserted sphere of different dielectric properties. This sphere has a diameter of 2 cm and has dielectric properties corresponding to muscle tissue heated to 44° C. Surrounding phantom has dielectric properties corresponding to the muscle tissue of body temperature (37° C). For simplicity, dispersive properties of biological tissues were not taken into account. Dielectric properties of the muscle phantom and the heated sphere were chosen according to fig. 2 and fig. 3, as values corresponding to the frequency of 2 GHz, as it is roughly center frequency of the analyzed spectrum. Different positions of the heated sphere were simulated as shown in fig. 15. Simulated s_{11} parameters were transformed into time domain using IDFT to obtain impulse response pairs $x_1(t)$, $x_2(t)$, where $x_1(t)$ corresponds to simulation without heated sphere, and $x_2(t)$ to simulation with heated sphere. (frequency windowing of s_{11} data was omitted in this trials). Magnitude of differential signals $\Delta x(t)$ obtained from $x_1(t)$ and $x_2(t)$ is shown in the fig. 16 and fig. 17. The magnitude of differential signals was normalized by the maximum module of the strongest of the compared differential signals. Time was recalculated to distance using Eq. 2.4. Results of the simulations show, that a dielectric inhomogeneity, corresponding to a change in the dielectric parameters of the muscle tissue when it is heated, can be detected by the proposed antenna. Arrival time of peaks of calculated differential signals is in good agreement with the expected arrival time, calculated from inhomogeneity distance, and permittivity of tissue (eq.2.4). From the results of simulations is further noticeable increase of sensitivity of the antenna at 45° deflection from the antenna axis (observable on signals belonging to sphere positions 2 and 3), although this effect seems to apply only in the immediate vicinity of the antenna as signals belonging to sphere positions 5 and 6 are nearly the same amplitude. By comparison of azimuth and elevation plane sensitivity of the antenna (at 45° deflection), it can be concluded that sensitivity seem to be slightly higher in the azimuthal plane.
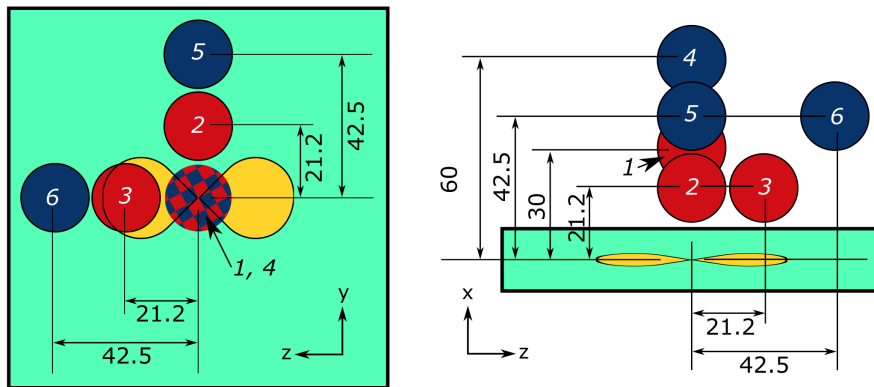

Fig. 15: Simulated positions of heated sphere relative to the antenna.
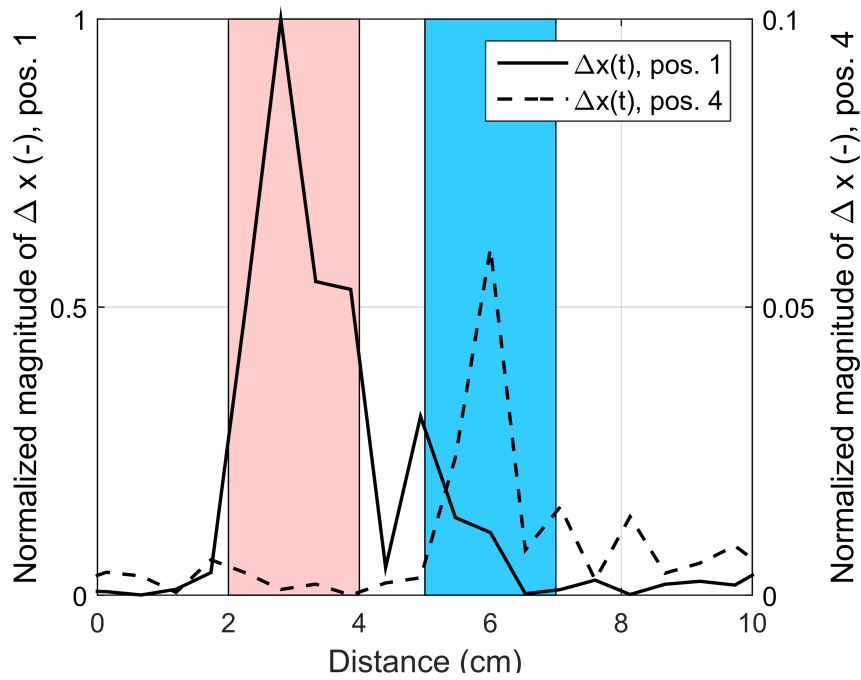
23

Fig. 16: The normalized magnitude of calculated differential signals, colored strip indicates the area of the heated sphere. Red strip - the center of the heated sphere in 30 mm distance, blue strip - the center of the heated sphere in 60 mm distance.
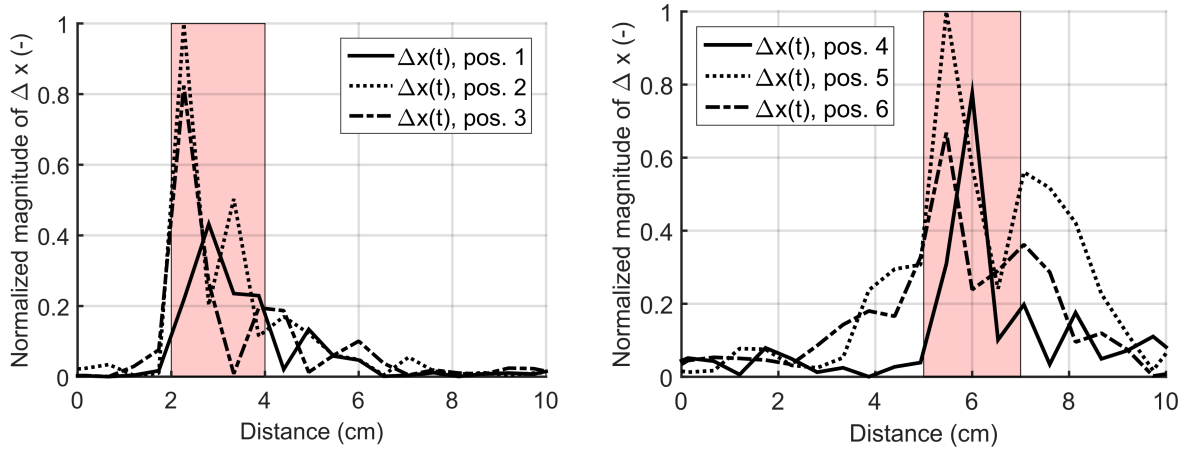

Fig. 17: The normalized magnitude of calculated differential signals, colored strip indicates the area of the heated sphere.

Chapter 6

Fabrication of designed bow-tie antenna

Since designed UWB antenna is composed of planar parts, standard PCB technology could have been used for antenna parts fabrication. Planar parts with conductive motives were fabricated on the substrates Rogers RO4003C of heights 1.524 mm (bow-tie arms) and 0.508 mm (UWB tapered balun). Planar parts for mechanical reinforcement of the antenna were fabricated from substrate Isola DURAVER 104 of height 2 mm. All planar parts needed for one antenna fabrication are shown in fig. 18. The mechanical connection between substrates was made by gluing with epoxy glue. Resulting fabricated antenna is shown in the detail in fig. 19. All eight fabricated antennas (as they are intended for multi-static imaging system presented in the following chapter) are shown in fig. 20.
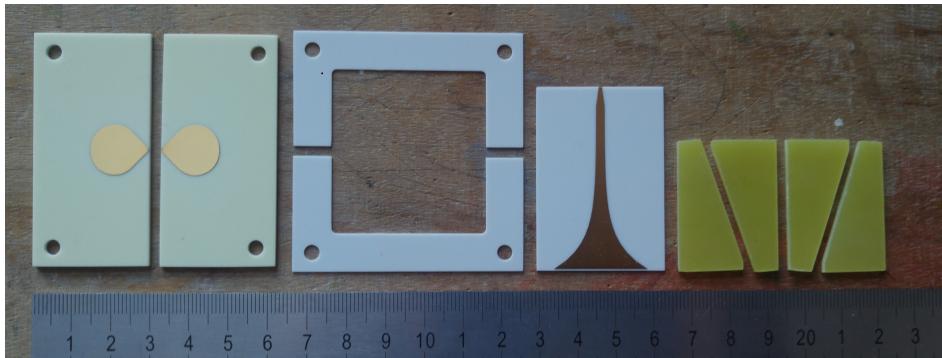

Fig. 18: Fabricated planar components intended for assembly of designed UWB antenna. From the left - bow-tie arms and auxiliary reinforcement (both RO4003C), UWB balun feeder (RO4003C) and mechanical reinforcement parts (Isola DURAVER 104).
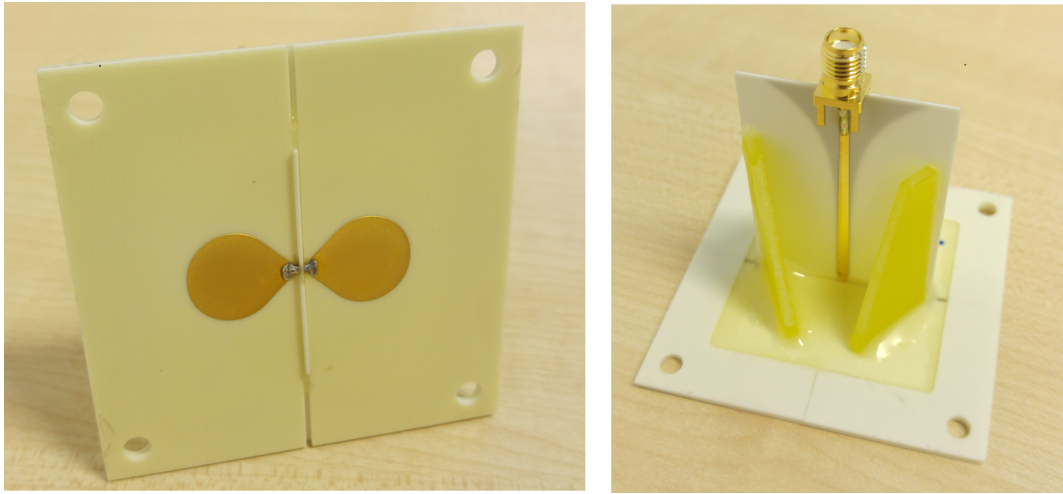
Fig. 19: Fabricated UWB bow-tie antenna with tapered balun feed.
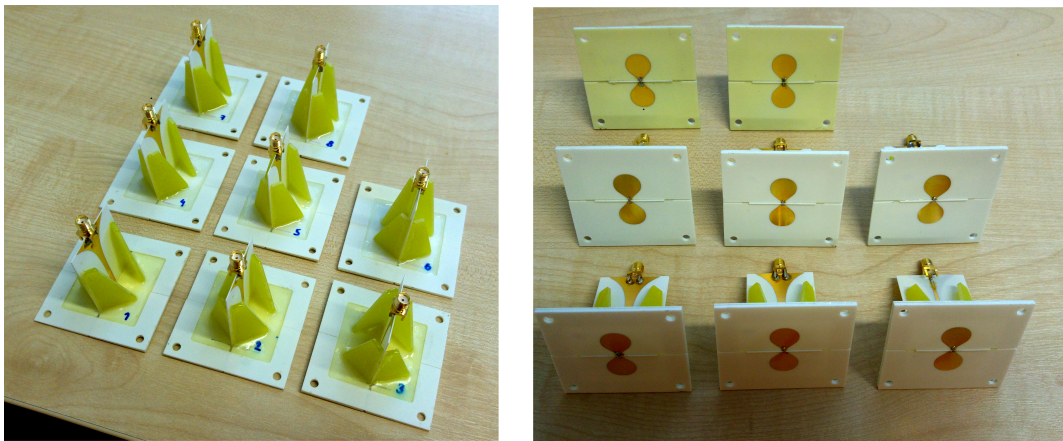

Fig. 20: All fabricated antennas.

Chapter 7

UWB radar system based on designed antenna

The designed antenna was used to build a UWB radar-based imaging system, consisting of 8 proposed antennas connected via semi-rigid coaxial cables to switching matrix controlled by VNA. Antennas are in this system attached to an octagonal plastic holder. On each wall of this holder is placed one of 8 antennas. Dimensions of the holder (showed in fig 21) are based on the dimensions of the average male European head. Dielectric properties of brain tissues are very similar to muscle tissue and so it is advantageous to use this shape, which (using a phantom of the brain) also allows this system to be used to investigation of stroke detection, a problem very similar to non-contact temperature measurement (in terms of microwave UWB radar-based detection).

Block diagram of the whole imaging system is shown in fig. 21. Transmission s-parameters of 8-port are measured using VNA and switching matrix, which allows measuring this 8-port without the need for cable switching. Frequency windowing is applied on measured s-parameters, and resulting frequency domain data are transformed into the time domain using IDFT, and thus obtaining impulse response matrix of the system (this process was described in more detail in chapter 2).

Since the differential measurement is performed (subtraction of impulse responses corresponding to the same channel but measured in a different time), performing vector calibration on antennas ports is not needed. However, it is necessary to eliminate the parasitic time delay of the measured impulse responses resulting from the signal propagation in the VNA and switching matrix circuits, in the coaxial cable and in the antenna supply circuit (in this case planar balun feeder). This delay can be calculated (and thus eliminated) using impulse responses, which contain antenna crosstalk (static clutter). As dielectric properties of phantom (biological tissue) can be quite accurately estimated, and so phase speed of propagating wave v_p (see eq. 2.4) and distance between each bow-tie pair is known, expected arrival time τ_{ab} of

antenna crosstalk between antennas a and b can be calculated as follows

$$\tau_{ab} = \frac{d_{ab}}{v_p} \tag{7.1}$$

Parasitic delay D on each of 8 ports can be then calculated by compiling 8 linear equations and solving them for known values of T_{ab} (crosstalk arrival time) and τ_{ab} (expected crosstalk arrival time) according to the following formula

$$\mathrm{T}_{ab} = D_a + D_b + \tau_{ab} \tag{7.2}$$

Calculated values of parasitic delay D of each port are then used to shift measured impulse responses x'_{ab} in time, to obtain delay-compensated impulse responses x_{ab}

$$
\begin{aligned}
x_{ab}(t) &= x'_{ab}\big(t - (D_a + D_b)\big) &&\text{for } t \geq (D_a + D_b) \\
x_{ab}(t) &= 0 &&\text{for } t < (D_a + D_b)
\end{aligned}
\tag{7.3}
$$

By subtracting $x_{ab}^{t_1}$ (impulse responses measured at $t = t1$) from the $x_{ab}^{t_2}$ (impulse responses measured at $t = t2$) differential signals Δx_{ab} are obtained. These signals are then processed with DAS algorithm to produce 2D scattering profile of the tissue (as described in chapter 2).
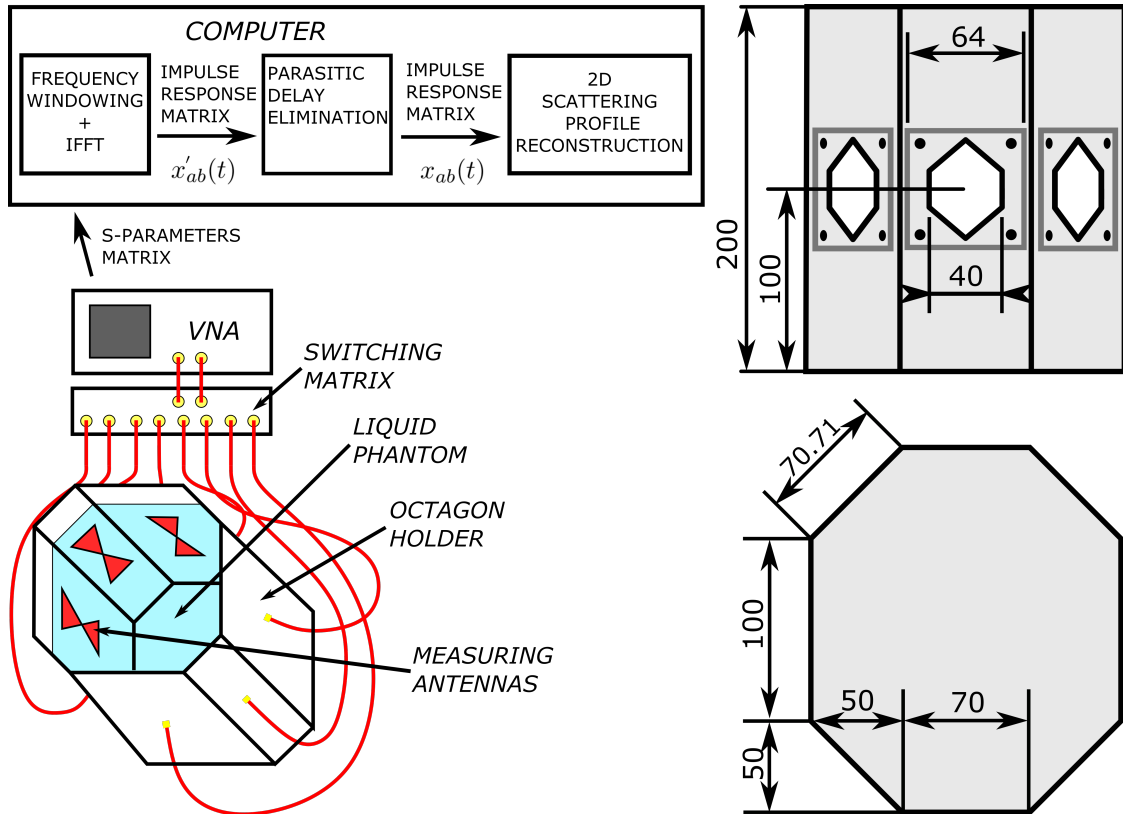

Fig. 21: On the left schematic picture of UWB radar-based imaging system for 2D measurement of scattering profile in liquid phantom. On the right dimensions of the octagonal plastic holder.

Chapter 8

Measurements

In this chapter, results of measurements taken with the designed antenna are presented. The first section presents the results of the s_{11} parameter measurement of all eight fabricated antennas. The second section provides results of measurement of SAR distribution in muscle phantom irradiated by the designed antenna. The last section shows the imaging capability of a UWB radar system built with the designed antennas, which was presented in the previous chapter.

8.1 Measurement of s_{11} parameter of the fabricated antennas

S_{11} parameter of all eight designed bow-tie dipoles was measured. Dipole surface was placed on the liquid muscle phantom. This phantom was prepared from isopropanol, distilled water, and salt. The relative permittivity of this phantom was adjusted to fit the dielectrical properties of muscle by selecting an appropriate ratio of water to isopropanol. Conductivity was then set by adding salt (NaCl). Dielectric properties of this phantom were measured using Dielectric Assessment Kit (DAK 12 probe) from SPEAG, which allows measuring of dielectric constant up to 3 GHz. Dielectric properties of the prepared liquid phantom are shown in fig. 22. The magnitude of s_{11} parameter of all 8 antennas is shown in the fig. 23. Results show good agreement with the simulation and also good stability among fabricated antennas. The magnitude of s_{11} parameter of antennas does not exceed -12 dB in the frequency band from 0.7 GHz up to 4.6 GHz.
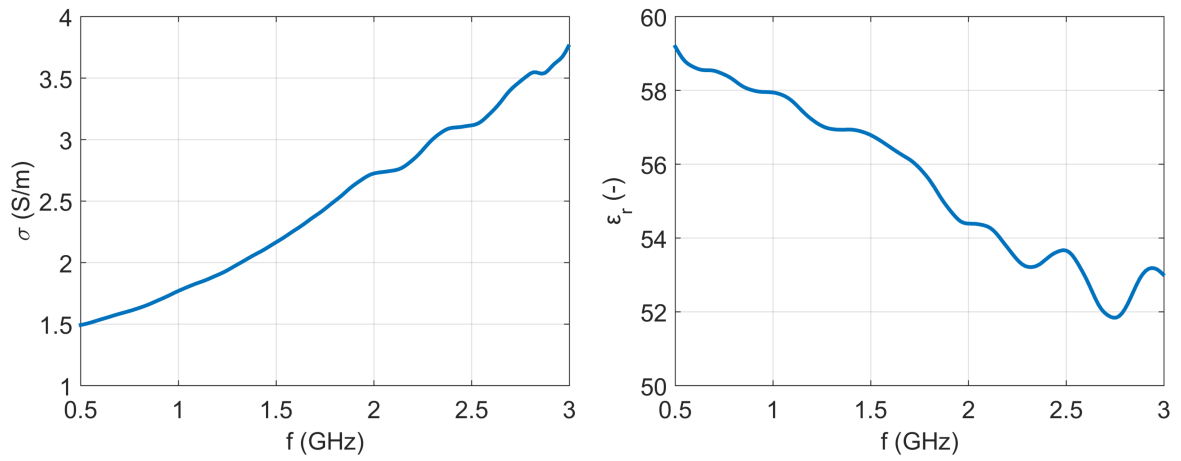
Fig. 22: Dielectric properties of liquid muscle phantom, prepared for the measurement of the s_{11} parameter of fabricated antennas.
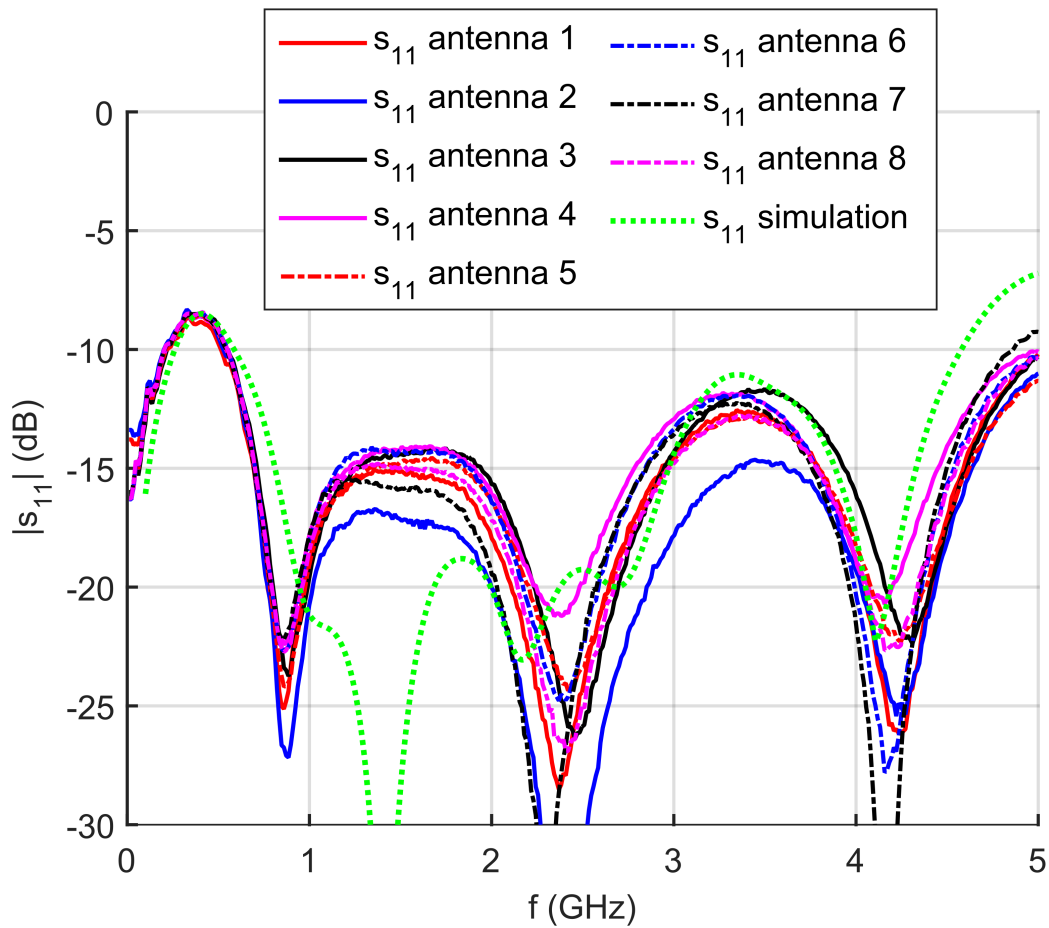

Fig. 23: The magnitude of the s_{11} parameter of the fabricated antennas attached to the muscle phantom.

8.2 Measurement of SAR distribution in muscle phantom

SAR (specific absorption rate), indicating the distribution of electromagnetic energy dissipation in a lossy environment, can be measured indirectly, either by measuring the temperature profile or by measuring the distribution of the electromagnetic field quantities (most often the electric field intensity). Since the measurement of electromagnetic field quantities is significantly demanding and requires a special measuring apparatus, the thermal profile measurement using a thermal camera was chosen to verify the SAR distribution. This approach is appropriate, if temperature profile is captured right after phantom heating (irradiation), which should be (as far as possible) performed in the shortest possible time interval to minimize the effect of heat conduction resulting from non-zero thermal conductivity of the phantom.

The measurement setup is shown in fig. 24. Antenna, attached to muscle phantom (prepared according to [4]), was connected to 40 Watt microwave generator working on frequency 2.45 GHz. The generator fed the antenna for 60 seconds. Immediately after the end of the heating process, the temperature profile of the phantom surface was captured on the thermal camera and so was captured temperature profile of the phantom cut. Results, presented in fig 25, show quite good agreement with simulated SAR distribution (presented in section 5.5) and show that the antenna can efficiently transmit microwave power to the tissue.
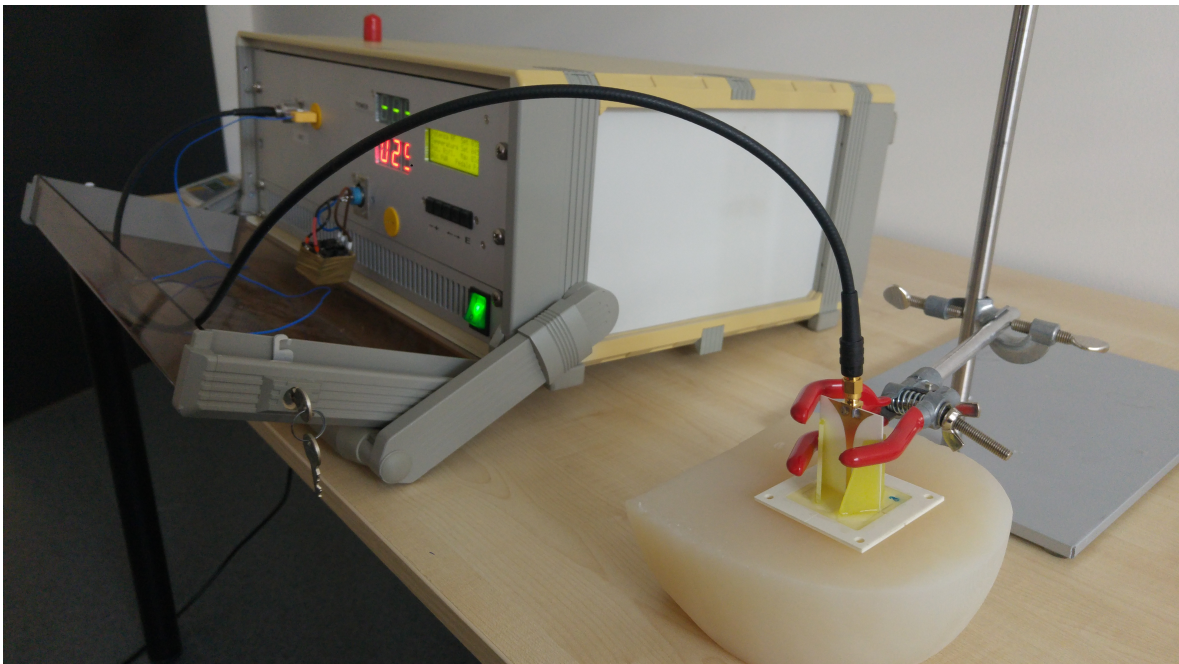

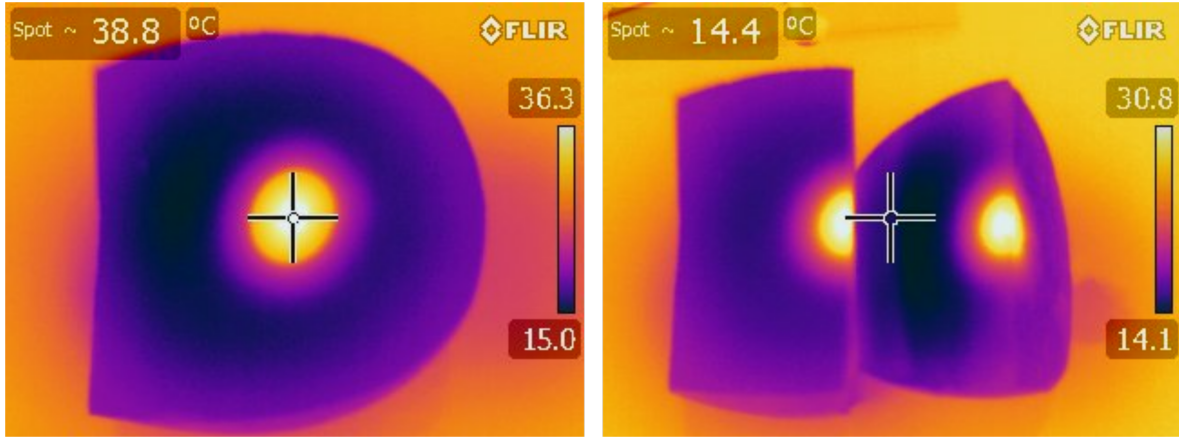Fig. 24: Setup for microwave heating of muscle phantom.

Fig. 25: Temperature distribution along the surface of the irradiated phantom (left) and along the phantom cut (right).

8.3 Measurement of scattering profile of phantom with inserted inhomogeneity

UWB radar-based imaging system presented in chapter 7 was built with the designed antennas. The system is shown in the fig. 26. Holder was filled with liquid phantom, which was described earlier and his dielectric properties are shown in fig. 22. The thin wall hollow cylinder was used to simulate dielectric inhomogeneity in muscle tissue. This cylinder (see fig. 26) has a diameter of 40 mm and was filled with distilled water. Three positions of this cylinder were measured to show system ability to reconstruct 2D scattering profile of the phantom, resp. ability to detect inhomogeneity within the analyzed region. Resulting profile was obtained by processing differential signals, which were produced by subtraction of measured impulse responses (scenario with inserted cylinder) from impulse responses measured without inserted cylinder (process described in the detail in chapter 7 and 2). Level of the liquid phantom was always kept the same to avoid signal changes other than those associated with embedded dielectric inhomogeneity. Two of three reconstructed scattering profiles shown in fig. 27 prove, that system is able to detect and locate such inhomogeneity, as cylinder position, determined by a red circle, is in good match with reconstructed scattering intensity profile. In one case system wasn't able to detect accurately cylinder position. A possible explanation could be imperfect sealing of holder, which caused continuous leaking of phantom liquid on feeding strip of one of measuring antennas, which position was the closest to this location of the cylinder inhomogeneity in that scenario, and thus could significantly affect the results of the scattering profile reconstruction.
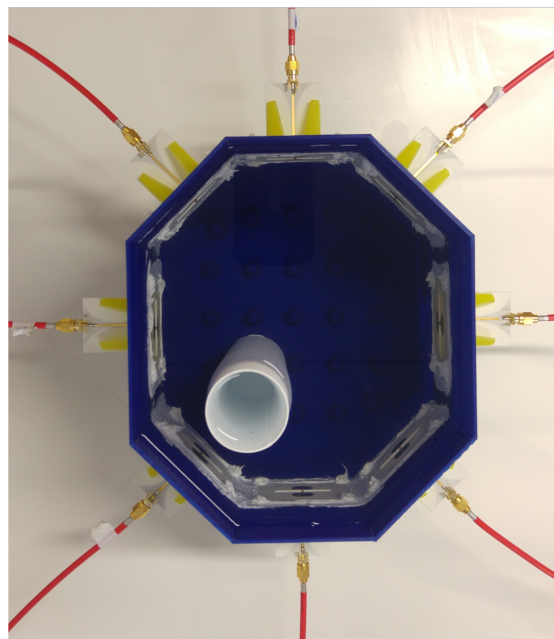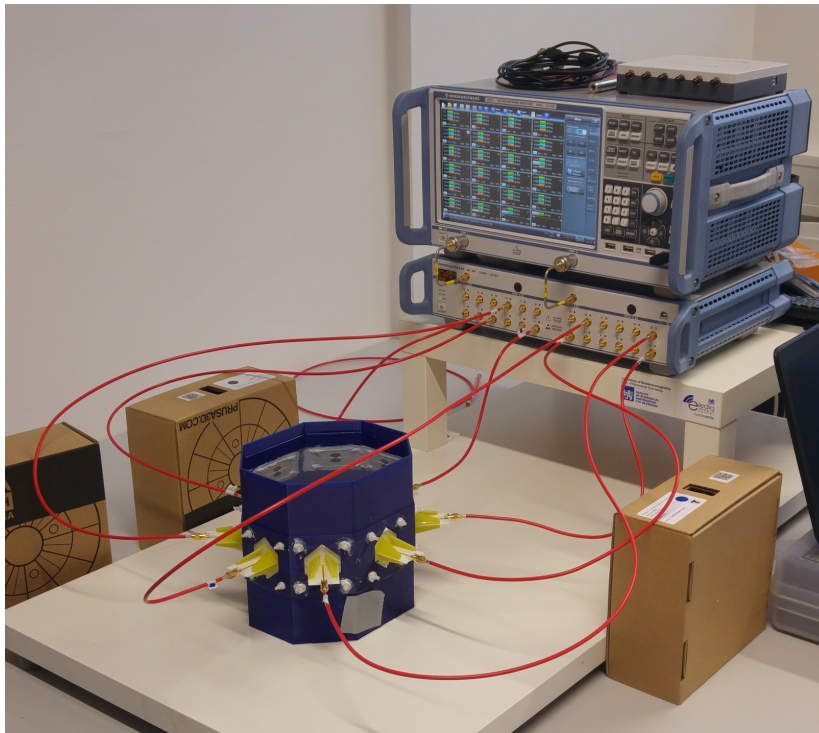
Fig. 26: Top - UWB radar-based imaging system composed of the designed antennas attached to the holder. Antennas are connected via switching matrix to VNA. Bottom - Cylindrical inhomogeneity composed of a plastic cylinder filled with distilled water inside holder filled with liquid phantom.

Fig. 27: Reconstructed scattering profile of liquid phantom with inserted cylindrical-shaped dielectric inhomogeneity. Position of this inhomogeneity is marked by the red circle. Positions of antennas are marked by red crosses and inner borders of the holder by a blue dashed line.

Chapter 9

Conclusion

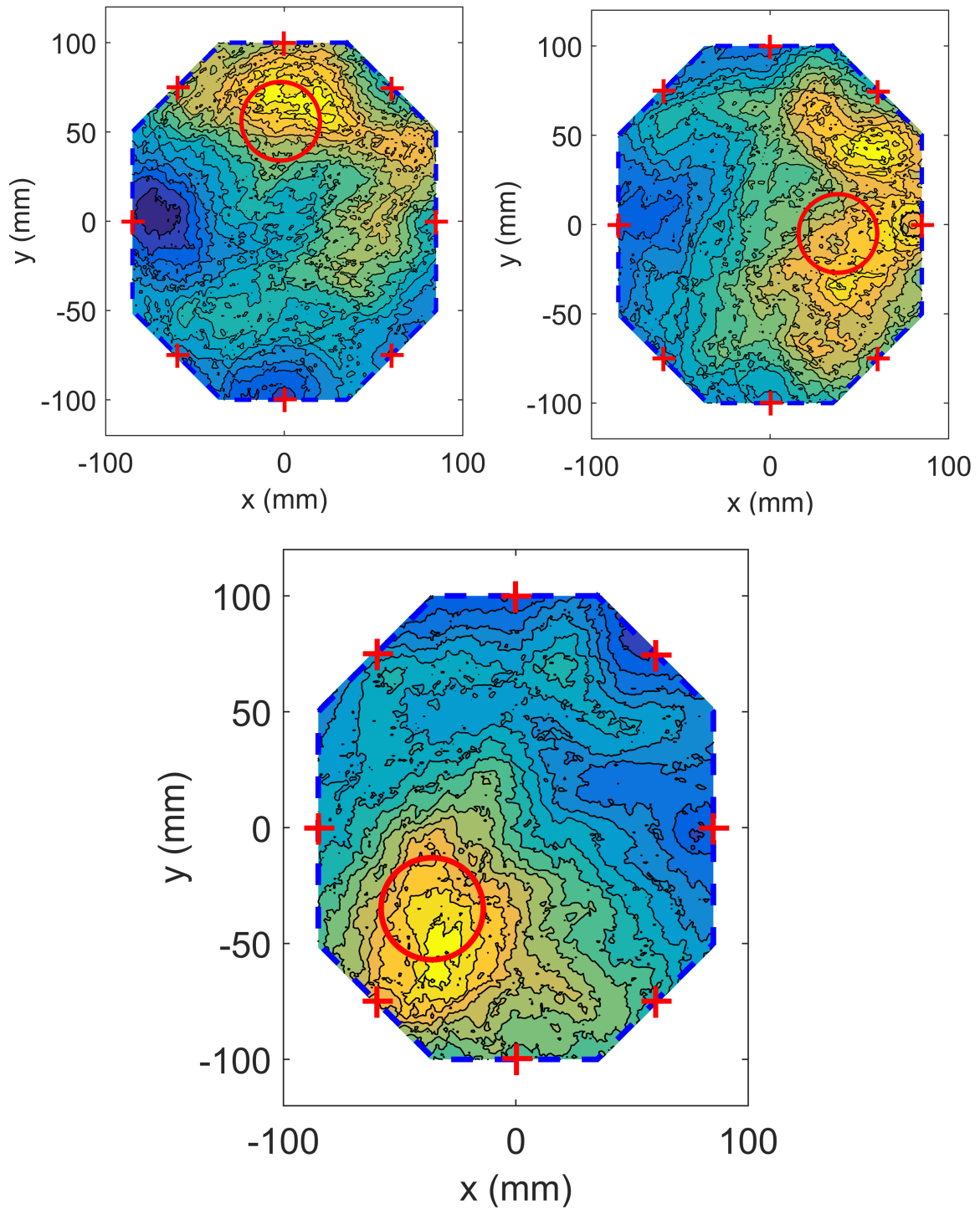In this work, the antenna for microwave imaging methods in medicine was designed. It is a dipole composed of planar parts, namely bow-tie arms and perpendicular ultra-wide balun feeder. Antenna structure was optimized in FDTD solver with respect to multiple performance demands, which imaging antenna should meet. Bow-tie arms shape was miniaturized by edge rounding as small dimensions of the antenna are advantageous in an imaging application. So was optimized the shape of transition balun to meet the condition of ultra-wide symmetrization resp. impedance matching. Possibility of temperature change detection using system with the designed antenna was shown using simulations, where a heated sphere was placed and consequently detected in various positions in muscle phantom model. The designed antenna was fabricated in a load of eight pieces, and s_{11} parameter of these antennas was measured. All fabricated dipoles are good impedance matched on muscle tissue, having a magnitude of s_{11} parameter below -12 dB from 0.7 GHz up to 4.7 GHz. Moreover, the stability of s_{11} parameter among fabricated antennas is very good. SAR in muscle phantom irradiated by the designed antenna was simulated and later measured using microwave generator working on frequency 2.45 GHz, to show antenna directional behavior in the near field and ability to effectively transmit microwave energy to muscle tissue. Proposed antennas were used to build microwave UWB radar-based imaging system. System ability to reconstruct scattering profile was tested using differential measurement. Plastic cylinder filled with distilled water was inserted to liquid muscle phantom and antenna s-parameters resp. differences within impulse responses obtained by transformation of s-parameters to time domain were measured. Results of the reconstructions showed that detection and location of dielectric inhomogeneity is by the proposed imaging system is possible.

Bibliography

[1] Fiser O., Helbig M., "Feasibility study of temperature change detection in phantom using M-sequence radar". *10th European Conference on Antennas and Propagation (EuCAP)*, 2016.

[2] Fiser O., Merunka I. "Microwave Hyperthermia System for Head and Neck Area with Noninvasive UWB Temperature Change Detection". *Progress In Electromagnetics Research Symposium - Spring (PIERS)*, 2017 .

[3] Fiser O., Hruby V. "Numerical Study of Differential Temperature Measurement in Human Muscle Tissue using UWB Radar". *Progress In Electromagnetics Research Symposium - Spring (PIERS)*, 2018.

[4] Kantova M., Fiser O., "High-Water Content Phantom for Microwave Imaging and Microwave Hyperthermia". *World Congress on Medical Physics and Biomedical Engineering*, 2018.

[5] Ley, S., Schilling S., "Ultra-Wideband Temperature Dependent Dielectric Spectroscopy of Porcine Tissue and Blood in the Microwave Frequency Range". *Sensors*, Vol. 19, Issue 7, 2019.

[6] Vrba, J. "Lékařské aplikace mikrovlnné techniky". *CTU in Prague, Faculty of Electrical engineering*, Prague, 2003.

[7] Conceicao R. C., Mohr J. J. 'An Introduction to Microwave Imaging for Breast Cancer Detection". *Springer*, ISBN 978-3-319-27866-7, 2016.

[8] Helbig M., Hilger I. "Experimental phantom trials for UWB breast cancer detection". *The 7th German Microwave Conference*, 2012 .

[9] Jalilvand M., Pancera E. "Hemorrhagic Stroke Detection via Adaptive UWB Medical Imaging Radar". *The 8th European Radar Conference*, 2011 .

[10] Latif S., Pistorius S. "A Double-ridged Horn Antenna Design in Canola Oil for Medical Imaging". *Proceedings of 2013 2nd International Conference on Advances in Electrical Engineering (ICAEE 2013)*, 2013.

[11] Latif S., Pistorius S. "Compact Ultra-Wideband Planar Tapered Slot Antenna for use in a Microwave Imaging System". *MICROWAVE AND OPTICAL TECHNOLOGY LETTERS*, Vol. 48, No. 11, November 2006.

[12] Gibbins D., Klemm M. "Design of a UWB Wide-Slot Antenna and a Hemispherical Array for Breast Imaging". *3rd European Conference on Antennas and Propagation*, 2009.

[13] Balanis C. A. "Modern Antenna Handbook". *John Wiley & Sons*, ISBN 978-0-470-03634-1, 2008.

[14] Karacolak T., Topsakal E. "A Double-Sided Rounded Bow-Tie Antenna (DSRBA) for UWB Communication". *IEEE Antennas and Wireless Propagation Letters*, Volume: 5, Page s: 446 - 449, 2006.

[15] Hasgall P., Neufeld E. "IT'IS database for thermal and electromagnetic parameters of biological tissues". *I_T_'I_S_ _F_o_u_n_d_a_t_i_o_n_*, 2017. [Online]. Achieavable on adress: www.itis.ethz.ch/database. [Cit.: 3. Jan. 2019].

[16] Helbig M., Kmec M., "Aspects of Antenna Array Configuration for UWB Breast Imaging". *6th European Conference on Antennas and Propagation (EUCAP)*, 2012

[17] Pastorino M., "Microwave Imaging". *John Wiley & Sons*, ISBN 9780470278000, 2010

[18] Stutzman W. L., Thiele G. A., "Antenna Theory and Design, 3rd Edition". *John Wiley & Sons*, ISBN: 978-0-470-57664-9, 2012

[19] Bourqui M., Okoniewski M., "Balanced Antipodal Vivaldi Antenna for Breast Cancer Detection". *The Second European Conference on Antennas and Propagation, (EuCAP)*, 2007.

[20] Xu Li., Hagness S. C., "Numerical and experimental investigation of an ultrawideband ridged pyramidal horn antenna with curved launching plane for pulse radiation". *IEEE Antennas and Wireless Propagation Letters*, vol. 2, Pages 259 - 262, 2003.

[21] Clemente F. S., Helbig M., "Permittivity-matched compact ceramic ultra-wideband horn antennas for biomedical diagnostics". *Proceedings of the 5th European Conference on Antennas and Propagation (EUCAP)*, 2011.

[22] Jafari H.M., Deen M. J., "A Study of Ultrawideband Antennas for Near-Field Imaging". *IEEE Transactions on Antennas and Propagation*, vol. 55, Issue 4, 2007.

[23] Zahirul Alam A. H. M., Rafiqul Islam M., "Design and analysis of UWB rectangular patch antenna". *Asia-Pacific Conference on Applied Electromagnetics*, 2007.

[24] Yurduseven O., Smith D., "Printed Slot Loaded Bow-Tie Antenna With Super Wideband Radiation Characteristics for Imaging Applications". *IEEE Transactions on Antennas and Propagation*, vol. 61, Issue 12, 2013.

[25] Kanj H., Popovic M., "Miniaturized microstrip-fed "Dark Eyes" antenna for near-field microwave sensing". *IEEE Antennas and Wireless Propagation Letters*, vol. 4, pages: 397 - 401, 2005.

[26] Qu W. S., Ruan C. L., "Effect of Round Corners on Bowtie Antennas". *PIER (Progress In Electromagnetics Research)*, vol. 57, pages: 179 - 195, 2006.

[27] Duncan J. W., Minerva V. P., "100:1 Bandwidth Balun Transformer". *Proceedings of IRE*, vol. 48, pages: 156 - 164, Issue 2, 1960.

[28] Kim S. G., Chang K., "Ultrawide-band transitions and new microwave components using double-sided parallel-strip lines". *IEEE Transactions on Microwave Theory and Techniques*, vol. 52, Issue 9, pages: 2148 - 2152, 2004.

[29] Carro P. L., Mingo J., "Electromagnetic Bandgap Microstrip to Parallel-strip Balun in Ultrawideband Applications". *38th European Microwave Conference*, 2008.

[30] Nguyen P. T., Abbosh A., "Wideband and compact quasi-Yagi antenna integrated with balun of microstrip to slotline transitions". *Electronics Letters*, vol. 49, isuue: 2, pages: 88 - 89, 2013.

[31] Sorokosz L., Zieniutycz W., " Proceedings of 21st International Conference Radioelektronika 2011". *Electronics Letters*, 2011.

[32] Carro P. L., Mingo J., " Analysis and Synthesis of Double-Sided Parallel-Strip Transitions". *IEEE Transactions on Microwave Theory and Techniques*,vol. 58, issue: 2, pages: 372 - 380, 2010.

[33] Algumaei M. Y., Shairi N. A., " Review of Mixer and Balun Designs for UWB Applications". *International Journal of Applied Engineering Research*,vol. 12, number: 17, pages: 6514 - 6522, 2017.

[34] Che W., Gu L., " Formula Derivation and Verification of Characteristic Impedance for Offset Double-Sided Parallel Strip Line (DSPSL)". *IEEE Microwave and Wireless Components Letters*,vol. 20, issue: 6, pages: 304 - 306, 2010.

[35] Chen J., " Double-sided parallel-strip line circuit analysis and applications to microwave component designs". *City University of Hong Kong*, Doctoral thesis, 2008. [Online]. Achieavable on adress: https://scholars.cityu.edu.hk/en/theses/theses(056cfb8e-0c44-4649-81a8-a6883e8969d3).html [Cit.: 21. March 2019].

[36] "Time Domain Measurements Using Vector Network Analyzers". *Application Note MS4640 Series VectorStar*, Anritsu, 2013.

[37] Nilavalan R., Gbedemah I., "Numerical investigation of breast tumour detection using multi-static radar". *Electronics Letters* Vol. 39 , Issue: 25 , 2003.